Theoretical investigation of mercury reactions with halogen species in the Arctic troposphere

Balakrishnan Viswanathan
Department of Chemistry
McGill University,
Montreal, Quebec H3A 2K6

September 2001

A thesis submitted to the Faculty of Graduate Studies and Research

in partial fulfilment of the requirements of the degree of

Master of Science

TABLE OF CONTENTS

ABSTRACT

Mercury is one of the most toxic elements present in the geosphere, present in many chemical and physical forms. Nearly uniform mixing ratios are observed within a hemisphere, the concentration being higher in the northern than in the Southern Hemisphere. Lack of kinetic data regarding mercury reactions prevents an explanation of the behaviour and deposition pathways of mercury from the atmosphere. Theoretical calculations have been carried out using DFT theory to investigate the thermodynamics and kinetics of the reactions of Hg^0 with Cl, Br, ClO, and BrO radicals and with Cl_2 and Br_2. The results from these calculations were used to evaluate the kinetic rate constants at 298.15 K and 238.15 K for the reactions involving gaseous mercury. In this paper, the results of this study are presented and relevance to the chemistry of the Arctic is discussed.

RÉSUMÉ

Existant sous de nombreuses formes chimiques et physiques, le mercure est l'un des éléments les plus toxiques de la géosphère. Des concentrations relatives plus ou moins uniformes peuvent être observées dans chaque hémisphère, avec une concentration plus élevée dans l'hémisphère Nord que dans l'hémisphère Sud. Le manque de données concernant la cinétique et la thermodynamique des réactions impliquant le mercure empêche d'expliquer son comportement et ses mécanismes de déposition dans l'atmosphère. La thermodynamique et la cinétique des réactions impliquant Hg^0 avec les radicaux Cl, Br ,ClO , BrO et avec Cl_2 et Br_2 ont été trouvées en utilisant plusieurs calculs numériques. Les résultats obtenus ont été utilisés pour évaluer les taux de réactions à 298.15 K et 238.15 K pour les réactions impliquant le mercure gazeux. Dans ce manuscrit, les résultats de cette étude sont présentés et ont été trouvés pertinents pour expliquer les observations sur terrain de la troposphère Arctique.

CHAPTER I: Introduction

1.1 Natural Abundance

Mercury exists mainly in the form of *epithermal* mineral deposits at comparatively shallow depths from the earth's surface. Many mercury minerals are known, these mainly being sulphides, halides, and even some amalgams (arquerite, moschellandsbergite, and konigsbergite). In addition, mercury minerals involving other main group and transition metal anions are also known. Cinnabar (HgS) is the predominant form of mercury and is hence the most commercially exploited source. Since cinnabar is commonly found in hot spring deposits, it is conjectured that mercury deposits are formed from hydrothermal solutions.[1]

1.2 Extraction and Uses

1.2.1 Extraction

Mercury deposits are largely recovered by underground mining methods, as the deposits are generally too small and irregular for open-pit mining methods to be economical. The normal method of extraction involves heating the ore or concentrate in retorts or furnaces to liberate the vapour which is then condensed. In the retort, the ore is mixed with either lime or iron and fired indirectly. Mercury is reduced in the following manner

$$4\ CaO + 4\ HgS \tau\ 4\ Hg + CaSO_4 + 3\ CaS \qquad (1.1a)$$

$$Fe + HgS \tau\ Hg + FeS \qquad (1.1b)$$

Furnacing is a process by which the ore and fuel are continuously fired in the same chamber and the mercury is obtained by

$$HgS + O_2 \tau Hg + SO_2 \qquad (1.1c)$$

1.2.2 Chloralkali Process

Historically, the principal industrial application of mercury has been to the simultaneous production of chlorine and caustic soda by the chloralkali process. This involves the electrolysis of brine solutions using a flowing cathode of metallic mercury. The sodium formed amalgamates with the mercury and is converted to NaOH with water. The mercury thus liberated is recycled into the cell. The process occurring in the cell is

$$NaCl \xrightarrow{electrolysis} \tau\ Cl_2\ (anode) + NaHg_x\ (cathode) \qquad (1.2a)$$

$$NaHg_x \xrightarrow{H2O} \tau\ NaOH + x\ Hg + \tfrac{1}{2}\ H_2 \qquad (1.2b)$$

Due to the losses of mercury (typically 150-250 g /1000 kg Cl_2) and the ill effects of mercury on health, this process is being gradually phased out world-wide. In fact, this method has already been banned in many nations.[1]

1.2.3 Electrical Industry

Mercury is widely used in fluorescent and high-intensity arc discharge lamps, rectifiers, oscillators, power control switches, hot-cathode tubes, and pool-cathode tubes for high-frequency applications. The majority of the mercury used in this category is devoted to the production of primary batteries, which have widespread use in domestic and industrial settings.[1] Since 1922, mercury has also been used in power stations as a means of generating electricity by the use of mercury vapour powered turbines. Since

mercury absorbs neutrons effectively, it has also been used as a shield for nuclear reactors.[2]

1.2.4 Other Uses

Metallic mercury finds use in a variety of common laboratory instruments such as barometers, manometers, thermometers, porosimeters, coulometers, diffusion pumps, Töpler pumps, air pumps, pump seals, mercury jet electrodes, and dropping electrodes. It has also been used in fuel cells and even as a vibration damper or coolant.[1] Mercury is also moderately used in the calibration of scientific glassware.[2] In addition to its use in instruments, mercury compounds are also used as catalysts in reactions, or for the catalytic production of laboratory catalysts.[1]

An important implementation of mercury used to be in the manufacture of mirrors. Mercury was used to amalgamate with tin and allows this foil to adhere to glass.[2] Taking advantage of their toxic properties, mercury compounds have in the past been used in such medical applications as diuretics, antiseptics, antisyphilitics, skin preparations and preservatives.[1]

1.3 Physical and Chemical Properties

Mercury is a dense (13,590 kg m^{-3} at 273 K) silvery liquid at ambient temperatures, melting at 234.3 K and boiling at 629.7 K.[3] It is also characterised by low electrical resistivity, high thermal conductivity, high surface tension, high thermal neutron capture cross section (360 barnes) and a uniform volume expansion over its

entire liquid range. Mercury attains a saturated concentration in air of 14 mg m^{-3} at 293 K and this increases to 72 mg m^{-3} at 373 K. The rate of vaporisation of purified mercury in still air is 7 $\mu g\ cm^{-2}\ hr^{-1}$.[4] The inorganic salts are sufficiently volatile that appreciable concentrations of mercury can form in the air in equilibrium with the salts. HgS, for example forms an equilibrium with 100 ng m^{-3} in dry air and nearly 50 times that amount in air with a relative humidity approaching 100 %, while dry air over HgO contains 2000 ng m^{-3}.[5] The relatively high volatility of mercury and its inorganic compounds suggests that atmospheric transport occurs on a substantial scale.

The first two ionisation potentials of mercury are higher than the other members of Group XII (Group II B). All members of this group exhibit the +2 oxidation state, but mercury alone exhibits a formal +1 oxidation state. This is due to the propensity of mercury to form strong Hg-Hg bonds. Polymercury cations containing linear chains of mercury in fractional oxidation states are also known. Due to its large size, the mercury atom is very polarisable. This property lends considerable covalent nature to the oxide, sulphide, and halides. Ionic lattices are restricted to the salts of the most electronegative anions like F^- and ClO_4^-. Thus, for example, $HgCl_2$ is largely covalent, existing as linear Cl-Hg-Cl monomers in the gas phase upto 1000 ®C and as undissociated $HgCl_2$ in aqueous solution.[6]

Mercury forms Hg-C linkages which are very stable in solution. In spite of their low bond energies (typically 20-30 kcal mol^{-1}), the low bond polarity along with the low affinity of mercury for oxygenated ligands leads to the low susceptibility of

organomercury complex hydrolysis. Electrophilic substitution occurs at the carbon in organomercury compounds and the propensity is greater for aryl compounds than alkyl compounds.

Mercury also forms strong linkages to sulphur-containing systems. This is evidence by the presence of very stable bis-mercaptides like the crystalline $Hg(SEt)_2$ compound. Sulphur bridging in $Hg(SBu^t)_2$ gives a polymeric structure with tetrahedrally co-ordinated mercury atoms.

1.4 Sources of Mercury in the Atmosphere

1.4.1 Natural Sources

The presence of relatively high levels of mercury in the air near mercury mines has been long observed. Volcanic gases and emissions from geothermal areas are also known to contain mercury vapour. It is estimated that the emissions from volcanoes are insignificant when compared to the two major sources, land degassing, and anthropogenic sources.

As mentioned earlier, mercury occurs in varying amounts in rocks and surface minerals around the world. Due to the volatility of the element and its compounds, mercury vapour is emitted continuously at rate depending on the mercury level in the soil, temperature, and barometric pressure. The total contribution to the atmospheric burden is estimated to be 1.78×10^{10} g yr^{-1} from degassing compared to 2×10^{7} g yr^{-1} from volcanic and geothermal sources.[5]

1.4.2 Anthropogenic Sources

By far the largest source of atmospheric mercury of anthropogenic origin is traced to the final consumption of mercury-containing manufactured goods. These include electrical equipment, batteries, pesticides, and pharmaceutical and dental uses. The next largest contribution is from the burning of fossil fuels. Coal, oil, and natural gas contain mercury in varying quantities and practically all of the mercury present is emitted as vapour. Chloralkali plants and municipal waste incineration used to be considerable sources of mercury, which are now being scaled back world-wide. The total anthropogenic contribution to the atmospheric load is estimated at 1.00×10^{10} g yr^{-1}.[5]

1.5 Effects of Exposure in Humans/Animals

1.5.1 Acute Mercurialism

Acute toxicity can occur from inhalation of mercury in milligram quantities. This is typified by symptoms of nausea, abdominal cramps, diarrhoea, muscle aches, fever, and an elevated blood cell count within a few hours. Higher exposures can lead to symptoms of pulmonary irritation with chest tightness, cough, and shortness of breath. Shortly after an acute exposure, the mouth and gums tend to redden and become sore. This is followed after a few days by the experience of a metallic taste along with further inflammation of the gums, loosening of the teeth, ulcers of the mouth, and a blue line at the gum margins. Occasionally, a tremor is noted.[2]

1.5.2 Toxicity from Chronic Exposure

1.5.2.1 Neurologic toxicity

The earliest finding that can be noted from chronic exposure to inorganic mercury is that of a tremor. Initially, only a fine, postural tremor is noted when the arms are outstretched. Increasing the exposure causes the tremor to increase in amplitude and coarseness. It also seems to be aggravated by intentional activities. If mercury exposure continues to the point of development of a significant tremor, a state of *erethism* may sometimes be observed. One who is affected easily becomes upset and embarrassed, irritable, and sometimes quarrelsome. This state is also accompanied by insomnia and nightmares, associated with depression and memory loss. Rarely, one experiences hallucinations, delusions, or mania.[2]

1.5.2.2 Kidney Toxicity

Inorganic mercury in the body is primarily stored in the proximal tubules of the kidney. It is therefore, not unexpected that the earliest signs of kidney damage would be manifested by a disorder of the proximal tubules. As these tubules are involved in the re-absorption of nutrients normally, filtered into the urine, tubular disease caused by mercury is expected to elevate the levels of glucose, phosphate, amino acids, and small molecular weight proteins in the urine.[2]

1.5.3 Behaviour in Biological Systems

There are four major reasons contributing to the unique biological behaviour of mercury as compared to the other members of Group XII (Group II B). The softness of

Hg^{2+} and RHg^{+} leads to a high affinity of mercurials for thiol groups. The combination of the high polarisability for mercury (by nature of its size) and its high polarising power (due to poor shielding from the $4f^{14}$ electrons) enhances the covalent nature of mercury compounds. This nature has implications for the bio-transport, distribution, and toxicity of mercurials. Mercury-carbon bonds exhibit very high stability. Both Hg^{2+} and RHg^{+} show a strong tendency to exhibit linear 2-co-ordinate stereo-chemistry in simple covalent compounds and complexes. Mercury has a greater reluctance than zinc and cadmium to form complexes in which the co-ordination number is greater than two.

Due to the affinity of RHg^{+} for sulphur ligands, simple thiol complexes RHgSR' are found to be very stable molecules. CH_3HgSCH_3 has been identified as a metabolite of methylmercury, having been identified in shellfish from Minamata Bay.[6] It is also conjectured that $(CH_3Hg)_2S$ might be involved in the cycling of organic and inorganic mercury in sulphur-rich sediments. It can be readily formed from CH_3Hg^{+} in the presence of $S^{=}$, and this may in turn decompose to HgS and dimethylmercury (DMM). It has also been shown that phenylmercury ($PhHg^{+}$) complexes with thiols decompose in solution to diphenylmercury (symmetrisation), which due to its lipid solubility and low polarity is expected to be a brain and nerve toxin.[6] The symmetrisation of dimethylmercury from methylmercury salts by thiols is not significant, but can be promoted by the presence of phosphines as

$$2\ MeHgX + 2\ PR_3 \lambda\ 2\ [MeHg(PR_3)]^{+}X^{-} \lambda\ Me_2Hg + HgX_2(PR_3)_2 \quad (1.3)$$

Mercury as Hg^{2+} also forms complexes with a large range of non-sulphhydryl amino acids (though it is obvious that complexes will be formed with sulphhydryl amino acids). ^{13}C and ^{1}H NMR, and infrared studies have suggested that the interactions occur through the N and O centres on these molecules.[6] Since mercury can interact with free amino acids, it is also expected that similar behaviour would be observed with proteins, and in fact, this is the case. As mentioned earlier, inorganic mercurials may react with one or two SH groups forming RSHgX or RSHgSR species. Hence, it can be seen that mercurials can affect the disulphide linkages in proteins to form linear S-Hg-S complexes, and it is conceivable that this may have an effect on the conformation (and hence, behaviour) of the protein. It is experimentally known that mercurials inactivate a large number of protein and enzyme functions, consistent with the known toxicity of these compounds.

1.6 Behaviour of Mercury in the Atmosphere

It is estimated that the lifetime of mercury in the atmosphere is of the order of 1-2 years, which leads to there being sufficient time for long range transport. This explains the observation of nearly uniform mixing ratios within a hemisphere, the concentration being higher in the Northern than in the Southern Hemisphere. This points to a mainly anthropogenic source for airborne mercury.

High-temporal-resolution measurements of total gaseous mercury in surface air at Alert, NWT, Canada (82.5° N, 62.3° W) show a recurring annual pattern characterised by distinct seasonal differences. TGM (total gaseous mercury) concentrations exhibit a large variability in spring, with frequent episodes of exceedingly low values. For a species

with such a long lifetime, such behaviour is most unexpected. Interestingly, the variability of mercury concentration is similar in form to the annual pattern of ozone depletion events that occur in the Arctic after polar sunrise. There is a fairly good correlation between the concentrations of gaseous mercury and ozone measured at this site.[7] There are two scenarios to explain the observations: (i) mercury and ozone react quickly and to completion in the period immediately following polar sunrise, or (ii) the mode of removal of mercury is similar to that of ozone, namely activation of halogens. The second scenario would entail oxidation of Hg^0 to Hg^{++} species, which are more water-soluble.

Atmospheric mercury is mainly found as elemental mercury (Hg^0) with concentrations in the range of 1-4 ng m^{-3} which accounts for over 90 % of the total airborne mercury. The concentration of mercury in precipitation varies between 1-50 ng L^{-1}, which is considerably larger [8] than that predicted from the Henry's Law constant (0.32 at 298 K)[9]. Hence, Hg^0 must be oxidised to water-soluble forms in the atmosphere. A variety of oxidants are available, and can be divided into two types, viz. those that are oxygen containing, and halogens. Oxidants of the former type include, in addition to oxygen and ozone, the nitrogen oxides, peroxides and hydroxide.[9] The water-soluble compounds of mercury represent about 3 % of the total gaseous mercury and generally exceed the particulate mercury concentration.[10]

The atmospheric chemistry of mercury, though predominantly gas phase, can be influenced by heterogeneous processes. The gas phase oxidation of mercury by ozone

has been studied by P'yankov [11] and Iverfeldt and Lindqvist.[12] The data obtained were recalculated by Schroeder et al. to yield values for the rate constant to be 4.9 x 10^{-18} cm^3 $molec^{-1}$ s^{-1} and 1.7 x 10^{-18} cm^3 $molec^{-1}$ s^{-1} respectively. P'yankov's data as analysed by Schroeder and co-workers suggests a ten-fold increase in the reaction rate for every 30 K decrease in temperature. There is also mention of a yellow/brown solid, which is likely HgO.

Hg^0 can also be oxidised to HgX_2 type compounds by H_2O_2 or molecular halogens. The reactions of the type

$$Hg_{(g)} + X_{2(g)} \delta HgX_{2(g)} \qquad (X = OH, Halogens) \qquad (1.4)$$

are found to be fairly exothermic for oxidation by H_2O_2 and halogens, and are therefore expected to be found extensively. The oxidation enthalpy ranges from –75 kJ mol^{-1} for H_2O_2 to –208 kJ mol^{-1} for Cl_2.[9]

When a mixture of halogens is present, there is the possibility of forming mixed halides of mercury. It is also possible for displacement reactions to occur. The reactions involving the chloro, bromo, and iodo complexes of mercury with halogens are found to be moderately thermodynamically favoured compared to the presence of the "pure" halides. The mercury halides are expected to be in both the gas phase and solid phase.

In the presence of moisture, there is a possibility of finding mercury halides in the aqueous (droplet) phase. This is because mercury is also oxidised in aqueous medium by oxidants such as ozone, HOCl/$^-$OCl (dissolved chlorine), and OH.[13] The aqueous oxidation of mercury by $^-$OCl/HOCl was studied by Lin and Pehkonen [13] at various pHs around neutral, and their kinetic data shows little dependence on the pH of the system. The second order rate constant (296-298 K) exhibits oscillation around a value of 2.0 x 10^6 M^{-1} s^{-1} at pH between 6.52 and 8.39. Estimation has been made of the rate of reaction between Hg^0 and Cl_2 in the gas phase and in the presence of water vapour to be 4 x 10^{-16} cm^3 $molecule^{-1}$ s^{-1}.[14] It is very much possible that the reported rate of reaction is a combination of the gas phase and solution phase reactions. Oxidation of Hg^0 to Hg^{++} in the aqueous phase is stimulated by the presence of Cl^-, and I^-, more so by I^- than Cl^-.[15] In addition to the above processes, the reduction of Hg^{++} to Hg^0 by SO_2 and HO_2 has also been reported. Aqueous reduction of Hg^{++} occurs through $HgSO_3$ and not through $Hg(HSO_3)_2$ or $Hg(SO_3)_2^=$.[16] The rate of reduction by sulphite is estimated to be 0.6 s^{-1}, this rate being dependent on the concentration of the $HgSO_3$ complex.[17] Van Loon and co-workers have measured the rate of the redox decomposition of $HgSO_3$ to be as small as (0.0106 ! 0.0009) s^{-1}.[18]

It is definitely unfortunate that the concentrations of TGM in the Arctic undergo rapid depletion events during the polar sunrise. This is bound to have adverse implications for the health of the inhabitants of circumpolar regions, which is of concern to the appropriate authorities. It is also worth pursuing as to what the cause of depletion might be. Since it has been seen that mercury levels are constant during the Arctic

winter, it is fairly obvious that the rate of deposition must balance the sources (emissions and transport). It follows then, that the depletion must be completely due to photochemical processes occurring during the polar sunrise. As mentioned earlier, the concentrations of mercury and ozone show a fairly good correlation. This would imply that either the mode of depletion of both is the same, or that mercury and ozone react with each other in a photo-induced reaction. It is known that if either Hg^0 or ozone were photo-excited, the oxidation would be enhanced.[19] It is also known that halogen species are involved in the depletion of ozone during the polar sunrise.[20-25] Hence, it is possible that both processes contribute to the observed depletion events involving mercury. This study focusses on the role of halogens in the oxidative deposition of mercury. To this end, the following two schemes have been proposed:

Scheme 1.1:

$$Hg + X \tau HgX \qquad (1.5a)$$

$$HgX + X\tau HgX_2 \qquad (1.5b)$$

$$Hg + X_2 \tau HgX_2 \qquad (1.5c)$$

Scheme 1.2:

$$Hg + XO \tau (HgOX)^A \qquad (1.6a)$$

$$(HgOX)^A \tau HgO + X \qquad (1.6b)$$

$$(HgOX)^A \tau HgX + O(^1D) \qquad (1.6c)$$

$$(HgOX)^A \tau HgOX \qquad (1.6d)$$

In the above, X refers to the halogens studied, which in this case are F, Cl, Br, and $(HgOX)^A$ is the transition state formed from the addition of halo-oxides to Hg. The species HgOX has not been observed experimentally, till date, but that is probably more a problem of the sampling techniques than the lack of existence of the species. This is because the speciation of mercury is not very well known and it is hence possible that the reactive intermediates in the mercury cycle may have been missed by the bulk measurement techniques.

This study is aimed at studying the behaviour of mercury in the gas phase, especially considering the amount of uncertainty surrounding the specifics of the system. This is particularly true of the speciation of the deposition phase containing mercury. This includes continuous (dark) deposition and the deposition occurring during the depletion events (believed to be photo-initiated or photo-mediated). The approach taken here is to determine the relative importance of various pathways by calculating the rates of reaction for the loss of gas-phase Hg^0. This leads to an identification of the important pathways involved in the depletion of gaseous mercury. Knowing the relative rate (factoring in the effect of second species concentration), the exact proportional speciation can be estimated. In order to estimate the feasibility of reactions with appreciable rate, an initial thermodynamic analysis is performed. It is generally accepted that exothermic reactions tend to have smaller activation barriers and hence have higher rates. The thermodynamic and kinetic analyses are performed based on the results of quantum chemical calculations using Gaussian 98.[26] The information obtained is used directly in the case of the thermodynamic estimation and compared to experimental data.[27,28] The

kinetic analysis is performed using the treatment developed for the Transition State Theory.[29] In cases where the reaction occurs without an activation barrier, calculations are carried out using the treatment of Holbrook *et al*[30] by considering the dissociation of the corresponding associated species.

CHAPTER II: Theoretical Background

2.1 Background

In order to complement laboratory investigations into the gaseous chemistry of Hg^0, theoretical calculations are also being carried out. The purpose of these calculations is to investigate the thermodynamics and kinetics of the reactions of Hg^0 with Cl, Br, ClO_x, and BrO_x radicals, such that is possible to gain insight into the behaviour of mercury in the planetary atmosphere.

It is now possible to calculate equilibrium geometries and energies for a large number of simple compounds. However, as of yet, mainly due to the lack of experimental data regarding transition states, it is rather difficult to calculate absolute reaction rates.

The simplest, yet a rather powerful technique is the Hartree-Fock method of calculation. Being an *ab initio* method, it takes into account all electrons, each occupying a unique spin-orbital. One of the main drawbacks of the Hartree-Fock approach is the fact that electron correlation is not accounted for. Correlation is the property of the electrons keeping separate by as large a distance as possible within the field of the nuclei. In other words, an electron at a certain position would prevent another electron from coming within a certain distance due to their mutual Coulombic repulsion. This leads to a stabilisation of the system due to reduced repulsive potentials, which is not accounted for under the model. The Hartree-Fock correlation energy is defined as the difference between the HF calculated energy and the true energy of the system. Correlation plays a

large role in lowering the energy of atoms with many and diffuse orbitals and hence it has been found to be inadequate in dealing with transition metal complexes.

Due to the inadequacy of the Hartree-Fock procedure for the purpose at hand, attention was directed to the density functional theory as a means of solving the problem. This approach is based on the premise that the energy of an electronic system is a functional of the electron density. This has been shown to be a valid notion by the theorems of Hohenberg and Kohn. The difficulty involved in performing a true *ab initio* DFT calculation has led to the generation of many models making use of Kohn-Sham orbitals, which are analogous to the Hartree-Fock wavefunctions. In order to save computing time, the basis functions for larger atoms are parameterised by approximating the core electrons by a potential function (ECP). For the atoms belonging to periods 5 and 6, relativistic effects make significant contributions to the behaviour of the system. Hence, basis sets with relativistic functions must be used when calculating molecules containing such large atoms, like mercury. However, due to the difficulty of calculation, and the time required to attain self-consistency, relativistic wavefunctions are not always included in desktop models. This is an unfortunate cause for the inability to obtain exact energies. In any case, the deviation between energies calculated by non-relativistic wavefunctions and experimental values is of the order of a few percent.

2.2 Theory

2.2.1 Density Functional Theory

Density functional theory has been in use in some form from the 1920s and dates back to the early work by Thomas, Fermi, Dirac, and Wigner. The theory developed by

Thomas and Fermi is a true density-functional theory as it expresses all contributions to the total energy, kinetic as well as electrostatic, in terms of the electron density.

The Hartree-Fock-Slater (X_α) method was one of the first DFT-based schemes to be used on multi-atomic electronic systems. This method has its origins in the work of Slater, who in 1951 proposed that the exchange-correlation potential could be represented by a function that is proportional to the 1/3 power of the electron density.

Both the Thomas-Fermi and X_α methods were at the time of their inceptions considered as useful models based on the notion that the energy of an electronic system can be expressed as in terms of its density. A formal proof of this notion came when Hohenberg and Kohn [31] showed that the ground-state energy of an electronic system is uniquely defined by its density, although the exact dependence is unknown. For an N-particle system interacting with a given inter-particle interaction, the Hamiltonian and thus the ground state wavefunction (and energy) are completely determined by specification of the external field $\phi(r)$. In other words, the ground state energy is a functional of $\phi(r)$. They showed that there is a one-to-one correspondence between external field $\phi(r)$ and the single-particle density $\rho(r)$ and that it is then possible to write the total ground state energy as a functional of $\rho(r)$,

$$E[\rho] = E_0[\rho] + \int dr\, \phi(r)\, \rho(r) \qquad (2.1)$$

where $E_0[\rho]$ is a functional that is independent of the external potential $\phi(r)$. Hohenberg and Kohn also proved a second theorem which showed that for any trial density $\rho(r)$ that satisfies $\int \rho(r)\, dr = N$,

$$E[\rho] \mu E_g \qquad (2.2)$$

where E_g is the true ground state energy, the equality being valid only when $\rho(r)$ is the true ground-state single-particle density. The Hohenberg-Kohn theorems apply specifically to the ground state and hence are strictly valid only at zero absolute temperature. The extension of these theorems to non-zero temperature was accomplished by Mermin, who showed that for a system at temperature T, chemical potential μ, and external single particle potential $v(r)$, there exists a functional $F[\rho(r)]$, independent of $v(r)$ and μ, such that the following functional

$$\Omega[\rho(r)] = F[\rho(r)] + \int dr[v(r) - \mu] \qquad (2.3)$$

is a minimum for the correct equilibrium density $\rho(r)$ subject to the external potential. [32]

Kohn and Sham [33] derived a set of one electron equations from which in principle, one could obtain the exact electron density and hence the total energy. The total energy of an N electron system can be written without approximations as

$$E_{el} = -\tfrac{1}{2} \Sigma_i \int \phi_i(r_1) \nabla^2 \phi_i(r_1)\, dr_1 + \Sigma_A Z_A/|R_A - r_1|\, \rho(r_1)\, dr_1 +$$

$$\tfrac{1}{2} \int \rho(r_1)\rho(r_2)/|r_1 - r_2|\, dr_1 dr_2 + E_{XC} \qquad (2.4)$$

The first term in the above equation corresponds to the kinetic energy of N non-interacting electrons with the same density $\rho(r_1) = \Sigma_i^{occ} \phi_i(r_1)\, \phi i(r1)$ as the actual system of interacting electrons. The second term accounts for the attraction between electrons and nuclei, and the third term for the Coulomb repulsion between the two charge distributions $\rho(r_1)$ and $\rho(r_2)$. The last term contains the exchange-correlation energy E_{XC}

which can be expressed in terms of the spherically averaged exchange-correlation hole functions $\rho_{XC}^{\gamma\tau}(r_1,s)$ as

$$E_{XC} = -4\pi/3 \, \Sigma_\gamma \Sigma_\tau \, \rho_1^{\gamma}(r_1) \, \rho_{XC}^{\gamma\tau}(r_1,s) \, dr_1 \, s^2 \, ds \qquad (2.5)$$

where the spin indices γ and τ run over both α-spin and β-spin and $s = |r_1 - r_2|$. The one-electron orbitals of Eq. (2.3) are solutions to the set of one-electron Kohn-Sham equations

$$[-\tfrac{1}{2} =_1^2 + Z_A/|R_A - r_1| + \circ\rho(r_2) \, dr_2/|r_1 - r_2| + V_{XC}]\phi_i(r_1) = \kappa_S\phi_i(r_1)$$

$$= \varepsilon_i\phi_i(r_1) \qquad (2.6)$$

where the exchange-correlation potential V_{XC} is given as the functional derivative of E_{XC} with respect to the density

$$V_{XC} = \delta E_{XC}[\rho]/\delta\rho \qquad (2.7)$$

The hole function $\rho_{XC}^{\gamma\tau}(r_1,s)$ contains all information about exchange and correlation between the interacting electrons as well as the influence of correlation on the kinetic energy. The interpretation of $\rho_{XC}^{\gamma\tau}(r_1,s)$ is that an electron at r_1 will to a certain extent prevent other electrons from approaching within a distance s. The extent of exclusion increases with the magnitude of $\rho_{XC}^{\gamma\tau}(r_1,s)$. Multiplying the Kohn-Sham equations

$$(-\tfrac{1}{2} =^2 + V_s(r))\phi_i(r) = \varepsilon_i\phi_i(r) \qquad (2.8)$$

by ϕ_i^* and summing over all the electrons, yields

$$V_s(r) = (1/\rho(r)) \, \Sigma_i^N \, \tfrac{1}{2} \, \phi_i^*(r) =^2\phi_i(r) + \varepsilon_i|\phi_i(r)|^2 \qquad (2.9)$$

The exact total energy of the system can be represented as

$$E = \langle T \rangle + \langle V \rangle + \tfrac{1}{2} \int \Gamma(1,2)/r_{12}\, d1d2 \qquad (2.10)$$

where T is the kinetic energy, V is the potential energy in the external field, and $\Gamma(1,2)$ is the simultaneous probability of finding an electron with co-ordinates 1 (position r_1 and spin s_1) and another electron with co-ordinates 2. The physics of the correlation phenomenon is exhibited by splitting off the uncorrelated probability, which is just the product of the one-electron probability densities.

$$\Gamma(1,2) = \rho(1)\rho(2) + \Gamma_{XC}(1,2) \qquad (2.11)$$

The exchange-correlation part of Γ describes how the probability of finding a second electron is modified by the presence of the first one. Using the language of the exchange-correlation hole surrounding the electron at 1 by using the conditional probability $\Gamma(1,2)/r(1)$ to find an electron at 2 when one is known to be at 1,

$$\rho^{cond}(2|1) = \rho(2) + \Gamma_{XC}(1,2)/\rho(1) \qquad (2.12)$$

The probability of the other electrons to be at 2 is the unconditional probability $\rho(2)$ plus the exchange-correlation hole $\Gamma_{XC}(1,2)/\rho(1)$ that the electron at 1 "digs" around itself in the unconditional density $\rho(2)$. The electron-electron part of the total energy may hence be written as

$$\begin{aligned} \langle W \rangle &= \tfrac{1}{2} \int (\rho(1)\rho(2)/r_{12})\, d1d2 + \tfrac{1}{2} \int \Gamma_{XC}(1,2)/r_{12}\, d1d2 \\ &= \tfrac{1}{2} \int \rho(1) \int \rho(2)/r_{12}\, d2d1 + \tfrac{1}{2} \int \rho(1) \int \{\Gamma_{XC}(1,2)/\rho(1)\}\{1/r_{12}\}\, d2d1 \\ &= \tfrac{1}{2} \int \rho(1)\, V_{Hartree}(1)\, d1 + \tfrac{1}{2} \int \rho(1) V_{hole}(1)\, d1 \\ &= E_{Hartree} + W_{XC} \end{aligned} \qquad (2.13)$$

The conditional electron density is customarily written in terms of the pair-correlation factor g(1,2)

$$\rho^{cond}(2|1) = g(1,2)\rho(2) = \rho(2) + \Gamma_{XC}(1,2)/\rho(1) \qquad (2.14)$$

The hole density is then written as

$$\rho^{hole}(2|1) = \{g(1,2)-1\}\rho(2) \qquad (2.15)$$

Thus,

$$W_{XC} = \tfrac{1}{2} \circ \rho(1)\{g(1,2) - 1\}\rho(2)/r_{12}\, d1d2 \qquad (2.16)$$

An alternative manner in which to write the total energy in a Kohn-Sham calculation would be

$$E = T_s[\rho] + \circ\, \rho(1)V(1)d1 + \tfrac{1}{2} \circ\, \rho(1)\rho(2)/r_{12}\, d1d2 + E_{XC} \qquad (2.17)$$

As the Kohn-Sham potential is uniquely determined by the density, so are the solutions to the one-electron Kohn-Sham equations. Therefore, the kinetic energy of the electrons described by Kohn-Sham orbitals is a functional of the density

$$T_s[\rho] = \Sigma_i^N \circ \phi_i^*[\rho](1)\,(-\tfrac{1}{2} =^2)\phi_i[\rho](1)\, d1 \qquad (2.18)$$

This follows directly from the Hohenberg-Kohn Theorem, since this theorem implies that the wavefunction of a non-degenerate system is a functional of the density, and therefore every expectation value is, including the kinetic energy. It is to be emphasised that the E_{XC} is different from the traditional quantum chemical definition of the exchange-correlation energy as being the sum of the Hartree-Fock exchange energy and the correlation energy, the latter being traditionally defined as the difference between

the exact and Hartree-Fock energies. Comparing Equations (2.17) and (2.10), it is clear that

$$E_{XC}[\rho] = T[\rho] - T_s[\rho] + W_{XC}$$
$$= T_{XC} + W_{XC} \qquad (2.19)$$

The fact that the exact kinetic energy <T> is a functional of r has been used to write the difference between the exact kinetic energy and the Kohn-Sham kinetic energy as the exchange-correlation contribution to T. It is to be noted that the KS exchange-correlation energy consists of a kinetic part and a pure exchange-correlation part of the electron-electron interaction energy. In contrast, the traditional definition $E_X^{HF} + E_{corr}$ contains corrections to the electron-nuclear and Hartree energies due to the difference of $\Delta\rho$ between exact and Hartree-Fock densities.

$$\Delta\rho = \rho(1) - \rho^{HF}(1)$$
$$E_X^{HF} + E_{corr} = E_X^{HF} + E - E^{HF}$$
$$= T[\rho] - T^{HF}$$
$$+ \int \Delta\rho(1)\, V(1)\, d1$$
$$+ \int \Delta\rho(1)\rho(2)/r_{12}\, d1d2 + \tfrac{1}{2} \int \Delta\rho(1)\Delta\rho(2)/r_{12}\, d1d2$$
$$+ W_{XC} \qquad (2.20)$$

The Kohn-Sham definition has the advantage that it only consists of the exchange-correlation corrections to the kinetic energy ($T[\rho] - T_s$) and electron-electron interaction energy (W_{XC}) and is not filled with other terms. These other terms such as the correlation correction to the electron-nuclear energy and the corrections to the Hartree

energy are often quite large. The traditional definition has the operational advantage that the reference Hartree-Fock energy does not contain unknown quantities and can be calculated to virtually arbitrary accuracy. This is definitely not the case for the Kohn-Sham system, E_{XC} and its functional derivative V_{XC} being known only approximately. Obtaining them exactly is equivalent to a full solution of the many-electron problem.

The physical significance of the Kohn-Sham potential $V_{XC}(r) = \delta E_{XC}/\delta\rho(r)$ can be realised by incorporating the kinetic energy part of an equation which is formally similar to Eq. (2.16), but in which the pair-correlation factor has been redefined by the coupling-constant integration (Eqs. 2.21 – 2.24). The coupling constant integrated hole is described by the "average" pair correlation factor g(1,2) in terms of which E_{XC} may be written as

$$E_{XC} = \tfrac{1}{2} \circ \rho(1)\{g(1,2) - 1\}\rho(2)/r_{12}\, d2d1$$

$$= \tfrac{1}{2} \circ \rho(1)\, V_{scr}(1)\, d1 \qquad (2.21)$$

The screening (or hole) potential V_{scr} is now due to an average exchange-correlation hole. It is referred to as the screening potential since the exchange-correlation effects embodied in g may be considered as screening effects on the full electron-electron interaction $1/r_{12}$. The considerations regarding exchange-correlation holes, on which present-day approximations for E_{XC} are based, almost always use the coupling constant integrated form. The Kohn-Sham potential

$$V_s(r) = V(r) + V_{Hartree}(r) + V_{XC} \qquad (2.22)$$

is related to E_{XC} since

$$V_{XC} = \delta E_{XC}/\delta\rho(r) \qquad (2.23)$$

Using Eq. 2.22, V_{XC} can be written as

$$V_{XC}(3) = \delta E_{XC}/\delta\rho(3) = V_{scr}(3) + V_{scr}^{response}(3) \qquad (2.24)$$

where

$$V_{scr}^{response}(3) = \tfrac{1}{2} \circ \rho(1)\, \delta g(1,2)/\delta\rho(3)\, \rho(2)\, d1d2 \qquad (2.25)$$

Eq. 2.24 demonstrates the physical nature of the components of V_{XC} and therefore of the Kohn-Sham potential. The most important part of V_{XC} is just the potential due to the averaged exchange-correlation hole. It is noteworthy that this part of V_{XC} is directly related to the exchange-correlation energy according to Eq. 2.21. In other words, the XC energy is half the screening potential.

$$E_{XC} = \circ\, \rho(r)\, \varepsilon_{XC}(r)\, dr = \tfrac{1}{2} \circ\, \rho(r)\, V_{scr}(r)\, dr \qquad (2.26)$$

V_{XC} contains, in addition to the screening potential, another term which has been called the response part. This is a measure of the sensitivity of the pair-correlation factor to density variations. The response potential does not affect the energy directly, but rather indirectly, as it determines, as part of the Kohn-Sham potential, the SCF density in the Kohn-Sham calculation. The response part of the potential has less pronounced features than the hole potential, but is required to obtain accurate Kohn-Sham orbitals and densities.[34]

2.3 Theoretical Methods used

2.3.1 B3LYP

The exchange-correlation energy of the Kohn-sham density functional theory is given by the "adiabatic connection" formula, which may be expressed as

$$E_{XC} = \int_0^1 U_{XC}^{\lambda}\, d\lambda \qquad (2.27)$$

where λ is an inter-electronic coupling-strength parameter that applies the $1/r_{12}$ Coulomb repulsion between electrons, and U_{XC}^{λ} is the potential energy of exchange-correlation at intermediate coupling strength the potential energy of exchange-correlation at intermediate coupling strength λ. This connects the non-interacting Kohn-Sham reference system ($\lambda = 0$) to the fully interacting real system ($\lambda=1$) through a continuum of partially interacting systems ($0 \leq \lambda \leq 1$), all of which share a common density ρ (the density of the real interacting system). Though the integrand explicitly refers to the potential energy only, the λ integration effectively generates the kinetic part of the exchange-correlation energy. The exchange-correlation potential energy U_{XC}^{0} at the $\lambda = 0$ lower limit (corresponding to the non-interacting Kohn-Sham reference system) is the pure exchange energy of the Kohn-Sham wavefunctions without dynamical correlation. This Kohn-Sham exchange energy will be designated E_X henceforth and is essentially, but not exactly, equal to the Hartree-Fock exchange energy.

The conventional exchange-correlation LSDA (local spin-density approximation) substitutes for each U_{XC}^{λ} a model value from local uniform-electron-gas theory. Unforunately, the local-electron-gas model is physically inappropriate near the $\lambda = 0$ exchange-only limit in molecular bonds. Hence, it is believed that the principal

source of the over-binding error of the LSDA is the $\lambda = 0$ end of the coupling strength integration.[35] Furthermore, Gunnarsson and Jones have stated that density-functional energy differences suffer conspicuous errors if there is a change in the number of orbital nodes. Local electron-gas models particularly poorly describe the intricacies of exact-exchange-energy differences corresponding to changes in orbital nodality. The problem is most acute at $\lambda = 0$.

Therefore, it is seen that exact exchange energy must play a role in highly accurate density functional approaches. Becke[35] proposed the exchange-correlation approximation

$$E_{XC} = E_{XC}^{LSDA} + a_0(E_X^{exact} - E_X^{LSDA}) + a_X\Delta E_X^{B88} + a_C\Delta E_C^{PW91} \qquad (2.28)$$

where a_0, a_X, and a_C are semi-empirical coefficients determined by an appropriate fit to experimental data. E_X^{exact} is the exact exchange energy, ΔE_X^{B88} is Becke's 1988 gradient correction to the LSDA for exchange, and ΔE_C^{PW91} is the 1991 gradient correction for correlation of Perdew and Wang. The electron gas parameterisation is used for the correlation component of the E_{XC}^{LSDA} term. The optimised values of the coefficients have been found to be

$$a_0 = 0.20 \; ; \; a_X = 0.72 \; ; \; a_C = 0.81 \qquad (2.29)$$

This functional is implemented in Gaussian G98W by substituting the following separable exchange and correlation functionals

$$E_{XC} = a_0E_X^{Slater} + (1-a_0)*E_X^{HF} + a_XE_X^{B88} + a_CE_C^{LYP} + (1- a_C)E_C^{VWN} \qquad (2.30)$$

The Vosko, Wilk, and Nusair 1980 correlation functional (VWN)[36] is used to provide the excess local correlation required, since LYP (correlation functional of Lee, Yang, and Parr, which includes both local and non-local terms)[37] contains a local term essentially equivalent to VWN.[38]

2.3.2 PW91

The correlation hole surrounding an electron is the real-space analysis of the correlation energy and its Fourier transform is the corresponding wave-vector analysis. The correlation hole of the uniform electron gas is commonly used in models for the hole in an inhomogeneous system and these models yield useful non-local density functionals for the correlation energy and potential.[39] The simplest construction is the random phase approximation (RPA) in which the Fourier transform of the hole is defined by an explicit frequency integral.

For a many-electron (N-electron) ground state with inhomogeneous spin densities $n_\mu(\mathbf{r})$ and $n_o(\mathbf{r})$, the total density at position $\mathbf{r}$ is

$$n = n_\mu + n_o \tag{2.31}$$

and the relative spin polarisation is

$$\zeta = (n_\mu + n_o)/n \tag{2.32}$$

The total correlation energy is then given by

$$E_c = \tfrac{1}{2} \int d^3r \int d^3r' \; \{n(\mathbf{r})\, n_c(\mathbf{r},\mathbf{r}')\}/|\mathbf{r}-\mathbf{r}'| \tag{2.33}$$

where $n_c(\mathbf{r},\mathbf{r}')$ is the density at $\mathbf{r}'$ of the correlation hole centred at $\mathbf{r}$, and obeys the rule

$$\int d^3r' \; n_c(\mathbf{r},\mathbf{r}') = 0 \tag{2.34}$$

The average correlation energy per electron

$$E_c/N = \frac{1}{2} \int_0^\infty dR\, 4\pi R^2\, \tilde{n}_c(R)/R \qquad (2.35)$$

is calculated using the average hole

$$\tilde{n}_c(R) = 1/N \int d^3r\, n(r) \int d\mathbf{R}'/4\pi\, n_c(\mathbf{r},\mathbf{r}+\mathbf{R}) \qquad (2.36)$$

where $d\mathbf{R}'$ is an angular element in **R** space. The Fourier analysis of the average hole is

$$\tilde{n}_c(R) = (1/2\pi)^3 \int_0^\infty dk\, 4\pi k^2\, \rho_c(k)\, \mathrm{Sin}(kR)/kR \qquad (2.37)$$

The average structure factor $\rho_c(k)$ is the Fourier transform of the average correlation hole and is given by

$$\rho_c(k) = \int_0^\infty dR\, 4\pi R^2\, \tilde{n}_c(R)\, \mathrm{Sin}(kR)/kR \qquad (2.38)$$

When $\tilde{n}_c(R)$ is sufficiently localised around R = 0, Equation 2.34 implies that

$$\lim_{k \to 0} \rho_c(k) = 0 \qquad (2.39)$$

Substitution of Equation 2.37 into Equation 2.35 yields

$$E_c/N = \int_0^\infty dk\, \rho_c(k) \qquad (2.40)$$

As can be seen from Equations 2.35 and 2.40, the real-space analysis decomposes the correlation energy into contributions from density fluctuations at different distances R, while the wave-vector analysis displays the contributions from fluctuations of wave vectors k. In a uniform electron gas, the relative spin polarisation ζ and density

$$n = 3/4\pi r_s^3 = k_F^3/3\pi^2 \qquad (2.41)$$

(where k_F is the Fermi wave vector) are independent of **r**, yielding

$$E_c/N = \varepsilon_c(r_s,\zeta) \qquad (2.42)$$

Applying the wave-vector analysis to the RPA, it can be shown that

$$\rho_c^{RPA}(k,r_s,\zeta) = -6Q^2/cr_s \int_0^{\infty} dW \{\alpha_\zeta(r_s,Q,W) - \ln[1 + \alpha_\zeta(r_s,Q,W)]\} \quad (2.43)$$

where

$$Q = k/2k_F \quad (2.44a)$$

$$W = \omega/2k_F^2 \quad (2.44b)$$

are the reduced wave vector and frequency respectively. In the above, $c = (4/9\pi)^{1/3}$ and the Fermi wave vector $k_F = 1/cr_s$. The α_ζ term is given by

$$\alpha_\zeta(r_s,Q,W) = cr_s/4\pi \, [x_1\beta(x_1Q,x_1^2W) + x_2\beta(x_2Q,x_2^2W)] \quad (2.45)$$

wherein

$$x_1 = (1 + \zeta)^{-1/3}$$

$$x_2 = (1 - \zeta)^{-1/3}$$

$$\beta(Q,W) = 1/Q^2 \{1+(W^2+Q^2-Q^4)/4Q^3 \ln[(W^2+Q^2(1+Q)^2)/(W^2+Q^2(1-Q)^2] -$$

$$W/Q[\mathrm{Tan}^{-1}((Q^2+Q)/W) - \mathrm{Tan}^{-1}((Q^2-Q)/W)\} \quad (2.46)$$

The Fourier transform of the exchange hole is

$$\rho_x(k,r_s,\zeta) = \tfrac{1}{2}(1+\zeta)F_x((1+\zeta)^{-1/3}Q) + \tfrac{1}{2}(1-\zeta)F_x((1-\zeta)^{-1/3}Q) \quad (2.47)$$

where

$$F_x(Q) = -1+3Q/2-Q^3/2 \qquad 0[Q[1 \quad (2.48)$$

$$= 0 \qquad Q>1$$

It is to be noted that the second derivative of F_x is discontinuous at Q=1. This is rectified in the Padé representation

$$F_x(Q) = -1/(1+1.5Q+2.25Q^2+2.875Q^3+3.5625Q^4+24.88Q^5) \quad (2.49)$$

which reproduces the first four derivatives of $F_x(Q)$ at Q=0 and also the integral of $F_x(Q)$ between 0 and ≡.[39] The small-wave-vector expansion of Equation 2.47 is

$$\rho_x(k,r_s,\zeta)\ \tau\ -1 + 3gQ/2 - Q^3/2 \qquad (2.50)$$

where

$$g(\zeta) = [(1+\zeta)^{2/3} + (1-\zeta)^{2/3}]/2 \qquad (2.51)$$

The local correlation energy ε_c has the small ζ expansion

$$\varepsilon_c(r_s,\zeta) = \varepsilon_c(r_s,0) + \tfrac{1}{2}\,\alpha_c(r_s)\zeta^2 + \ldots \qquad (2.52)$$

The small r_s or high-density expansion is

$$\varepsilon_c(r_s,\zeta) = c_0(\zeta)\ln r_s - c_1(\zeta) + c_2(\zeta)\, r_s \ln r_s - c_3(\zeta)\, r_s + \ldots \qquad (2.53)$$

The large r_s or low-density expansion is

$$\varepsilon_c(r_s,\zeta) = -d_0(\zeta)/r_s^{\,p} + d_1(\zeta)/r_s^{\,2p-1/2} \qquad (2.54)$$

The exact correlation energy has p=1, but within the scope of the RPA treatment, the correct exponent is p=¾.[39,40] On the basis of numerical evaluation of RPA integrals, Vosko *et al.* [36] propose the spin interpolation formula

$$\varepsilon_c(r_s,\zeta) = \varepsilon_c(r_s,0)+\alpha_c(r_s)\ f(\zeta)/f''(0)\ (1-\zeta^4)+\{\varepsilon_c(r_s,1)-\varepsilon_c(r_s,0)\}\, f(\zeta)\zeta^4 \qquad (2.55a)$$

$$f(\zeta) = \{(1+\zeta)^{4/3} + (1-\zeta)^{4/3} - 2\}/(2^{4/3} - 2) \qquad (2.55b)$$

It is noted that f(0) = 0, f(1) = 1, and f''(0) = 1.7909921. Instead of the more complicated analytic form of Vosko *et al.*[36] for $\varepsilon_c(r_s,1)$, $\varepsilon_c(r_s,0)$ and $-\alpha_c(r_s)$, Perdew and Wang recommend the following function:

$$G(r_s,A,\alpha_1,\beta_1,\beta_2,\beta_3,\beta_4,p) = -2A(1+\alpha_1 r_s)\ \ln\{1+\ 1/2A(\beta_1 r_s^{1/2}+\beta_2 r_s+\beta_3 r_s^{3/2}+\beta_4 r_s^{p+1})\} \qquad (2.56)$$

The parameters A, β_1, β_2 are chosen to match the exact high-density expansion (Equation 53) for which c_0 and c_1 are known.[36] Hence,

$$A = c_0 \tag{2.57a}$$

$$\beta_1 = (1/2c_0)\exp(-c_1/2c_0) \tag{2.57b}$$

$$\beta_2 = 2A\beta_1^2 \tag{2.57c}$$

It can then be found that

$$c_2 = A\alpha_1 \tag{2.57d}$$

$$c_3 = -2A\{\alpha_1 \ln(2A\beta_1) - (\beta_2/\beta_1)^2 + \beta_3/\beta_1\} \tag{2.57e}$$

The low-density expansion is then fixed, using *p*,

$$d_0 = \alpha_1/\beta_4 \tag{2.57f}$$

$$d_1 = \alpha_1\beta_3/\beta_4^2 \tag{2.57g}$$

As $\varepsilon_c(r_s,0)$, $\varepsilon_c(r_s,1)$, and $-\alpha_c(r_s)$ are known exactly from the VWN calculation[36], the terms α_1, β_3, and β_4 are adjusted to minimise the sum of squared errors

$$\Sigma_{rs}|G(r_s,\ldots) - a(r_s)|^2 \tag{2.58}$$

The resulting fit over the range $0.5<r_s<100$ had a maximum error of only 0.2 mRy (2 Ry = 1 Hartree).[40] It is thus concluded that this approach gives good results as compared to the VWN approach at a fraction of the computing time, as the system has also been re-parameterised. Some drawbacks of the VWN approach, namely the improper

behaviour at the high-density limit have been corrected conceptually.[40] The correlation potential for electrons of spin s is then

$$\mu_c^{\sigma}(r_s,\zeta) = \varepsilon_c(r_s,\zeta) - r_s/3 \neq\varepsilon_c(r_s,\zeta)/\neq r_s - (\zeta\text{-sgn}\sigma) \neq\varepsilon_c(r_s,\zeta)/\neq\zeta \qquad (2.59)$$

where sgnσ is +1 for $\sigma = \mu$ and −1 for $\sigma = o$.

2.3.3 QCISD

Unlike the other methods used in this study, QCISD (Quadratic Configuration Interaction including Single and Double substitutions) is not a density a functional method, but a post-Hartree-Fock multi-determinant method. Aside from Møller-Plesset perturbation methods, post-Hartree-Fock methods typically attempt to correct for correlation effects by employing multi-determinant techniques. It is to be recognised that even with orbital expansion in a finite basis, a full configuration interaction (FCI) solution is only possible for small systems. Therefore, approximate methods are required to solve larger systems while taking into account correlation effects. A model should then have the following characteristics:

i. It should be well defined, leading to a unique energy for any nuclear configuration and a continuous potential surface.

ii. It should be size consistent, or calculate energies should be additive when applied to an ensemble of molecules.

iii. It should be exact (equivalent to FCI) when applied to a two-electron system.

iv. It should be efficient so that application to large basis sets is not prohibitive.

v. It should give an adequate approximation to the FCI result.

vi. It should be variational, so that the computed energy is an upper bound to the correct energy.

The theoretical techniques discussed begin with the Hartree-Fock single-determinant wave equation

$$\Psi_0 = (n!)^{-½} \det\{\chi_1,\ldots,\chi_n\} \qquad (2.60)$$

where χ_i (i = 1,...,n) are the occupied spin-orbitals. χ_i is an eigenfunction of the one-electron Fock operator F with eigenvalue ε. The remaining eigenfunctions and eigenvalues of F are χ_a, ε_a (a = n+1,n+2,...,N; where N is the dimension of the basis).The symbols i,j,k,... and a,b,c,... refer to the occupied and virtual spin orbitals respectively. Other determinantal wave functions are derived from Ψ_0 by substitution of occupied spin orbitals by virtual spin orbitals. The single, double, and triple substitution operators can be defined as

$$T_1 = \Sigma_{ia}\, a_i^a\, t_i^a$$

$$T_2 = ¼\, \Sigma_{ij}^{ab}\, a_{ij}^{ab}\, t_{ij}^{ab}$$

$$T_3 = 1/36\, \Sigma_{ijk}^{abc}\, a_{ijk}^{abc}\, t_{ijk}^{abc} \qquad (2.61)$$

where t_i^a, t_{ij}^{ab}, etc. are elementary substitution operators and the a arrays involve undetermined coefficients. The operators act only on anti-symmetric determinants and hence the a arrays will be taken to be anti-symmetric in both the occupied and virtual suffixes. Various types of anti-symmetric wave functions can be obtained by applying various functions of the T operators to Ψ_0,

$$\Psi = f(T_1,T_2,\ldots)\Psi_0 \qquad (2.62)$$

and then determining the unknown a coefficients by appropriate projection of the Schrödinger function $(H-E)\Psi$, where H is the full Hamiltonian and E the full energy.

The simplest choice for the configuration function f is linear, yielding the configuration interaction wave functions

$$\Psi_{CID} = (1 + T_2)\Psi_0$$

$$\Psi_{CISD} = (1 + T_1+T_2)\Psi_0 \qquad (2.63)$$

It is useful to define

$$E = E_{HF} + E_{correlation}$$

$$H' = H - E_{HF} \qquad (2.64)$$

The CISD projection operators then are

$$\langle\Psi_0|H|T_2\Psi_0\rangle = E_{correlation} \qquad (2.65a)$$

$$\langle\Psi_i^a|H'|(T_1+T_2)\Psi_0\rangle = a_i^a\, E_{correlation} \qquad (2.65b)$$

$$\langle\Psi_{ij}^{ab}|H'|(1+T_1+T_2)\Psi_0\rangle = a_{ij}^{ab}\, E_{correlation} \qquad (2.65c)$$

The CISD energy emerging from the above equations is not size-consistent as the right-hand sides of Equations (2.65b) and (2.65c) are quadratic in the a vectors, whereas the left-hand sides are linear. The simplest method of correcting this inconsistency is to add terms quadratic in T_1, T_2 to the left hand side of Equations (2.65b) and (2.65c) to eliminate the term involving $E_{correlation}$. This yields

$$\langle\Psi_0|H|T_2\Psi_0\rangle = E_{correlation} \qquad (2.66a)$$

$$\langle \Psi_i^a | H' | (T_1+T_2+T_1T_2)\Psi_0 \rangle = a_i^a \, E_{correlation} \qquad (2.66b)$$

$$\langle \Psi_{ij}^{ab} | H' | (1+T_1+T_2+\tfrac{1}{2}T_2^2)\Psi_0 \rangle = a_{ij}^{ab} \, E_{correlation} \qquad (2.66c)$$

It can then be shown that

$$E_{correlation} = \tfrac{1}{4} \Sigma_{ijab} \, (ij||ab) \, a_{ij}^{ab} \qquad (2.67)$$

where

$$(ij||ab) = \int\int \chi^*_i(1) \, \chi^*_j(2) \, (1/r_{12}) \, [\chi_a(1)\chi_b(2) - \chi_b(1)\chi_a(2)] d\tau_1 d\tau_2 \qquad (2.68)$$

The QCISD method thus obtained was tested using first row systems against the coupled cluster method CCSD which was already prevalent at the time and was found to yield slightly better deviations from the results of FCI calculations performed on the same systems.[41]

2.4 Basis Sets used

2.4.1 LanL2DZ

The LanL2DZ basis set prepared by Hay and Wadt consists of an effective core potential (ECP) substituting for all the "core" electrons and only the "valence" electrons are explicitly defined. The ECPs were generated by obtaining numerical valence orbitals (ϕ_l) from self-consistent Hartree-Fock calculations. From these were derived smooth, nodeless pseudo-orbitals (ϕ'_l) in a manner so that these behave in as close a manner to the ϕ_l as possible, especially in the outer region of the atom. Numerical effective core potentials (U_l) were then derived for each angular momentum quantum number by

mandating that ϕ'_l is a solution in the field of U_l with the same orbital energy ε_l as ϕ_l. The numerical potentials were fit in analytic form with Gaussian functions. The numerical pseudo-orbitals (ϕ'_l) were also fit with Gaussian functions to obtain the set of basis functions.

The advantage of using a basis set with ECP is that computation of molecular properties can be achieved at a fraction of the computational cost involved in calculating with an all-electron basis set. Since this ECP was generated using *ab initio* all-electron wavefunctions, it is assumed that the ECP is a true substitute to, and closely reproduces the results from an all-electron basis. However, the results will diverge from all-electron cases if either of two cases is true. ECPs are unable to incorporate the effects of relaxation in sub-valence orbitals if such effects contribute to the molecular properties being calculated. In addition, if the core orbitals overlap between two atomic centres, the expression for the core-core interaction will break down leading to spurious bond lengths and other properties.[42]

2.4.2 6-311G

The 6-311G basis set is a split-valence basis set. This is chosen to give the lowest possible energy of the atomic ground state at the second-order Møller-Plesset (UMP2) perturbation level. The triple split (311) for the valence basis functions is associated with a six-Gaussian inner shell. The valence shell is split into three functions, represented by three, one, and one GTOs (Gaussian Type Orbitals). Five uncontracted *d*-functions are used for polarisation functions on non-hydrogen atoms.[43]

CHAPTER III: Thermochemical Investigation of Mercury Reactions

3.1 Introduction

The theoretical study of mercury compounds and reactions is non-trivial because (i) it has 80 electrons and hence the computing cost of an all-electron calculation is prohibitive, and (ii) the presence of 5d electrons available to perform chemistry causes relativistic effects to be important. In light of the above, it is imperative that a means be found to balance the increase in computing time and an increase in the accuracy of the model. It is obvious that an improvement in model accuracy naturally leads to an increase in computing time.

Model accuracy can be improved in two ways. One is to improve the theoretical model (method), and the other is to improve the mathematical representation of the atoms (basis set). There are presently two commonly used families of methods, namely Hartree-Fock based (*ab initio*) and Kohn-Sham based (density functional) methods. Direct Hartree-Fock methods are inappropriate for the calculation of mercury based systems. Cundari *et al.* reported smaller reaction enthalpies than those experimentally observed for the activation of methane by mercury complexes.[44] Hu and co-workers reported the binding energy for the HgO complex to be approximately three-quarters of the experimentally measured value.[45]

Post-Hartree-Fock methods including the M●ller-Plesset perturbation (MPn, where n=2-5) and coupled-cluster (CCSD and CCSD-T) methods seem to perform better

than direct Hartree-Fock calculations. Barone *et al.* report a good general agreement between their calculations carried out with the MP2 method and experimental results. They also note that the experiments were carried out in the solution phase and hence no direct comparison is possible.[46] Jonas and Thiel mention that MP2 has difficulties when calculating highly charged cations of Period 6 transition metals.[47] However, Luna-Garcia and others report a good behaviour of MP2 for the insertion of Cd and Hg (^3P) into SiH_4.[48] Coupled cluster (CCSD and CCSD-T) and configuration interaction methods (QCISD, QCISD-T, and CISD), due to their more extensive methods of treatment, yield better results than the M●ller-Plesset methods. For example, the spectroscopic constants of Hg_2 $^1\Sigma_g^+$ ground state have been well reproduced by each of these methods.[49] The disadvantage of these methods is that they are very computationally expensive techniques due to their thoroughness.

The density functional (DFT) methods have gained popularity in recent due to the availability of improved functionals producing better results, and the fact that these methods are computationally less expensive than the post-Hartree-Fock techniques yielding similar results. Jonas and Thiel report that the BP86 DFT method and CCSD(T) yield very similar results (as compared to experiment and to each other) for the dicarbonyl and dicyanide complexes of Au, Hg, and Tl.[47] Liu and co-workers also found that the four first ionisation potentials of atomic mercury are well reproduced by DFT calculations.[50] The fact that DFT works well even for solid state systems was utilised by Koper and van Santen who applied this technique to the interaction of halogens with Ag, Hg, and Pt surfaces. The dipole moment curves produced therein suggest a mainly ionic

interaction as suggested by theory.[51] Unfortunately, these techniques have a tendency of overestimating bond lengths as mentioned by Lupinetti *et al.*[52] Considering that DFT methods yield good energetic results and appropriate behavioural trends, in spite of the overestimation of bond lengths, it has been decided to perform the present study using density functional methods.

3.2 Computational Details

Calculations are carried out with the Gaussian 98 package.[26] Geometry optimisations are carried out at the B3LYP and PW91 levels of theory with the LanL2DZ basis set as implemented in Gaussian 98. All stationary points were confirmed by harmonic frequency calculations at the same level of theory. This basis set uses all-electron representation for the first-row elements, the heavier elements are represented with an effective core potential for inner electrons and double-zeta quality valence functions. Additional calculations are also performed using LanL2DZ for Hg alone and 6-311G(d) for O and all halogens (except I, which is not defined under that scheme). This latter basis set is an all-electron Gaussian-type basis-set incorporating d-function type polarisation for the valence shell. Further studies were conducted extending the polarisation to two sets of d-type polarisation and one set of f-type polarisation (2df). All calculations are carried out using spin-unrestricted wavefunctions to facilitate inter-comparison between closed-shell and radical species involved in this work.

3.3 Results

3.3.1 X and X_2 species

The geometries of the various species were optimised to an energy minimum and a harmonic frequency calculation was carried out to confirm the optimised geometry. The geometries calculated have been presented in Table 3.1. Comparison with other works and experimental data are presented where available. The symmetric dihalides were found to be linear and hence bond angles are not presented.

Table 3.1: Bond lengths of $Hg-X_n$ species in the gas phase.

Species	**Bond Length (Å)**				
	B3LYP/LanL2DZ	*PW91/LanL2DZ*	*Other Works* [b]		*Experimental*
HgO	2.044	2.033	2.00[a]		2.03[a]
HgF	2.173	2.186	2.10	2.06	
HgF_2	2.045	2.062	1.97	1.965	
HgCl	2.612	2.614	2.46	2.41	
$HgCl_2$	2.442	2.452	2.31	2.293	2.252[c]
HgBr	2.781	2.774	2.60		
$HgBr_2$	2.583	2.590	2.45	2.421	2.526[c]
HgI	2.980	2.963	2.80		
HgI_2	2.747	2.753	2.63	2.621	2.553[c]

[a] [45]

[b] [53] except where specified.

[c] [28]

Table 3.1 displays a fair correlation between the bond lengths calculated here and those calculated by other authors. Similarly, it is seen that the calculated bond lengths are generally longer than those measured experimentally. This is because electron correlation is explicitly treated under DFT techniques, without adequately accounting for

self-interaction. The standard reaction enthalpies were calculated as the difference between the standard enthalpy of each species, with the appropriate sign. The thermodynamics of the reactions of mercury with halogen species are presented in Table 3.2 below. The data is compared with data from the NIST Chemistry Web-book.[27]

Table 3.2: Reaction Enthalpies of reactions of Hg with halogen species.

Reaction	**Reaction Enthalpy ($-\Delta H$/kJ mol^{-1})**		
	B3LYP/LanL2DZ	*PW91/LanL2DZ*	*Experiment*
Hg + F τ HgF	152.91	192.21	137.84
Hg +F_2 τ HgF_2	354.57	354.69	355.03
HgF + F τ HgF_2	316.50	352.29	375.97
Hg + Cl τ HgCl	105.43	130.59	104.23
Hg + Cl_2 τ $HgCl_2$	230.33	237.03	207.67
HgCl + Cl τ $HgCl_2$	259.32	282.62	346.05
Hg + Br τ HgBr	80.12	103.55	69.06
Hg + Br_2 τ $HgBr_2$	180.12	188.53	146.83
HgBr + Br τ $HgBr_2$	227.39	250.33	301.50
Hg + I τ HgI	58.90	80.79	34.67
Hg + I_2 τ HgI_2	144.75	155.04	77.51
HgI + I τ HgI_2	202.92	225.23	256.36

It can be seen above that reaction enthalpy tends to be over-estimated by both calculation techniques, with the results of B3LYP/LanL2DZ being closer to the experimental values than those obtained from PW91/LanL2DZ calculations. In order to verify the similarity between experimental and calculated reaction enthalpies, and also to determine if there is a trend, the calculated enthalpies were plotted against the experimental enthalpies. The results obtained are presented below in Plot 3.1.

Plot 3.1: Comparison of calculated with experimental reaction enthalpies.

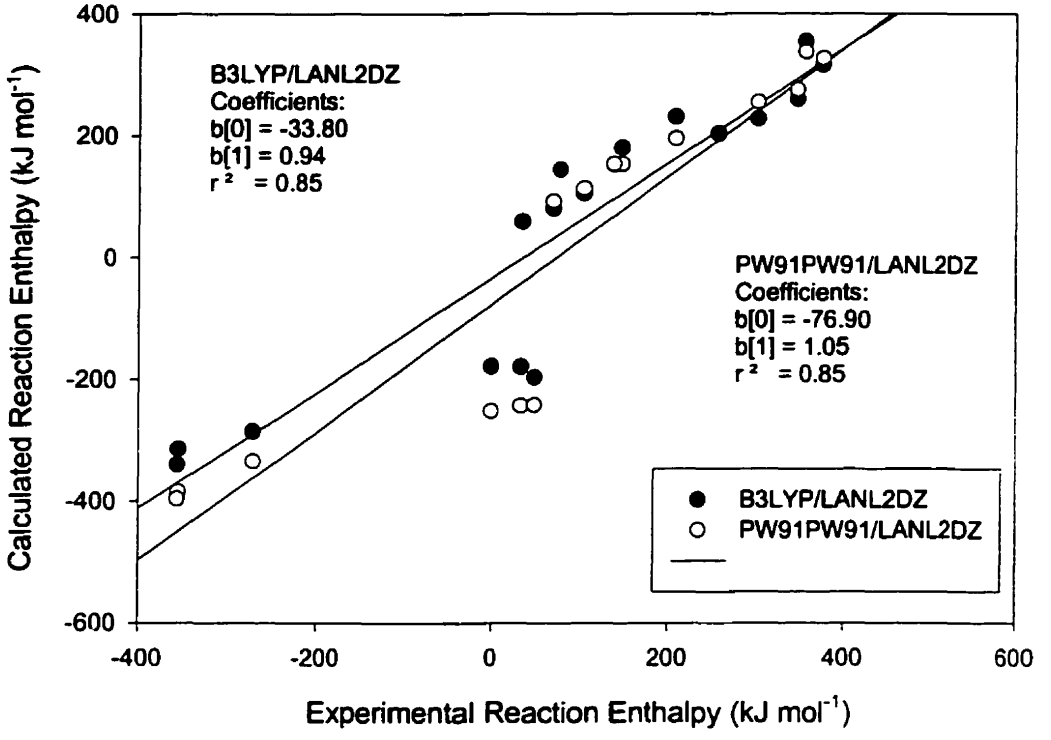

It can be seen from the above that there is a reasonable correlation of the calculated reaction enthalpies with the corresponding experimental reaction enthalpies. It is also seen that the two theoretical methods give similar results as compared to each other. The electronic energy level of each of the reactant and product species was plotted normalised relative to the reactants. The reaction scheme followed is:

$$Hg_{(g)} + X_{2(g)} \tau Hg_{(g)} + 2X_{(g)} \tau HgX_{(g)} + X_{(g)} \tau HgX_{2(g)} \qquad (3.1)$$

The results are presented in Plots 3.2 and 3.3.

Plot 3.2: Relative energy levels of $Hg + X_2 \tau Hg + 2X \tau HgX + X \tau HgX_2$ normalised relative to $Hg + X_2$ at the B3LYP/LanL2DZ level of theory.

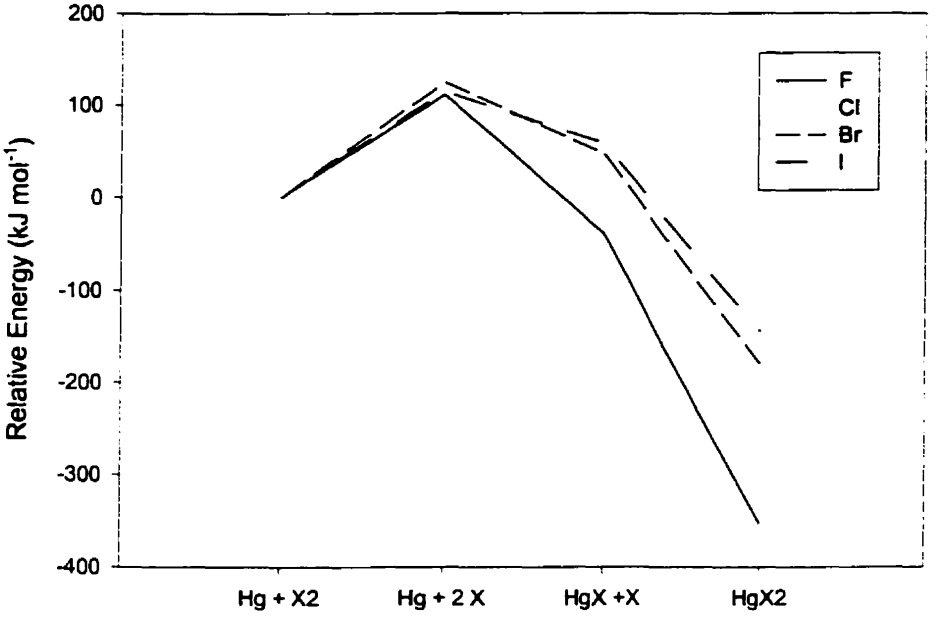

Plot 3.3: Relative energy levels of Hg + X_2 τ Hg + 2X τ HgX + X τ HgX_2 normalised relative to Hg + X_2 at the PW91/LanL2DZ level of theory.

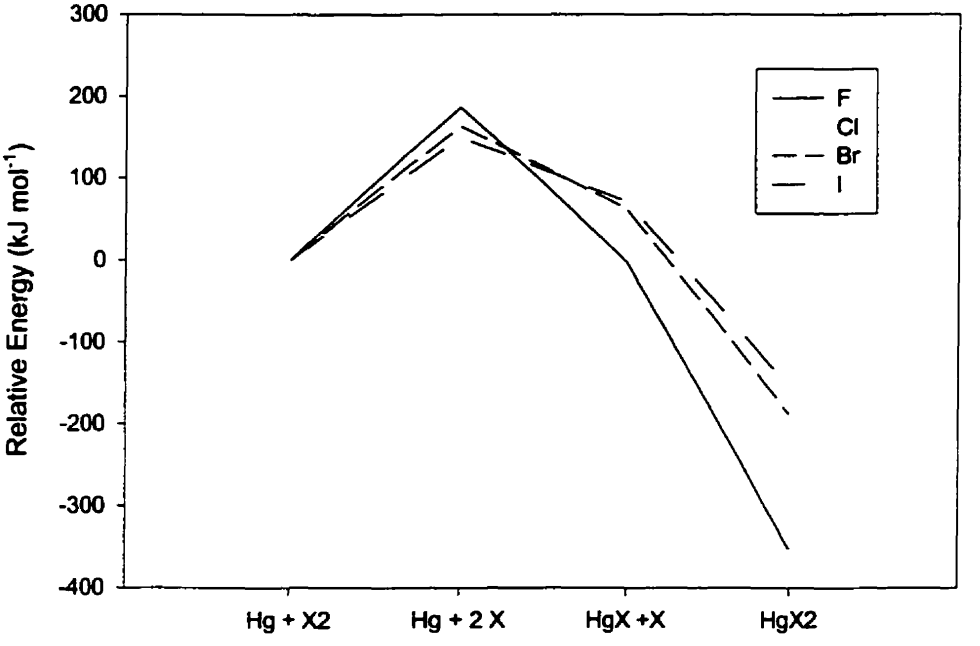

As is obvious from the above plots, the same general trend is observed in both systems. It is also seen that there is a difference in the magnitude of the effect observed. These can be compared with a similar plot prepared using data from the NIST database. This data is presented in Plot 3.4 below.

Plot 3.4: Relative energy levels of Hg + X_2 τ Hg + 2X τ HgX + X τ HgX_2 normalised relative to Hg + X_2 from the data available from NIST.

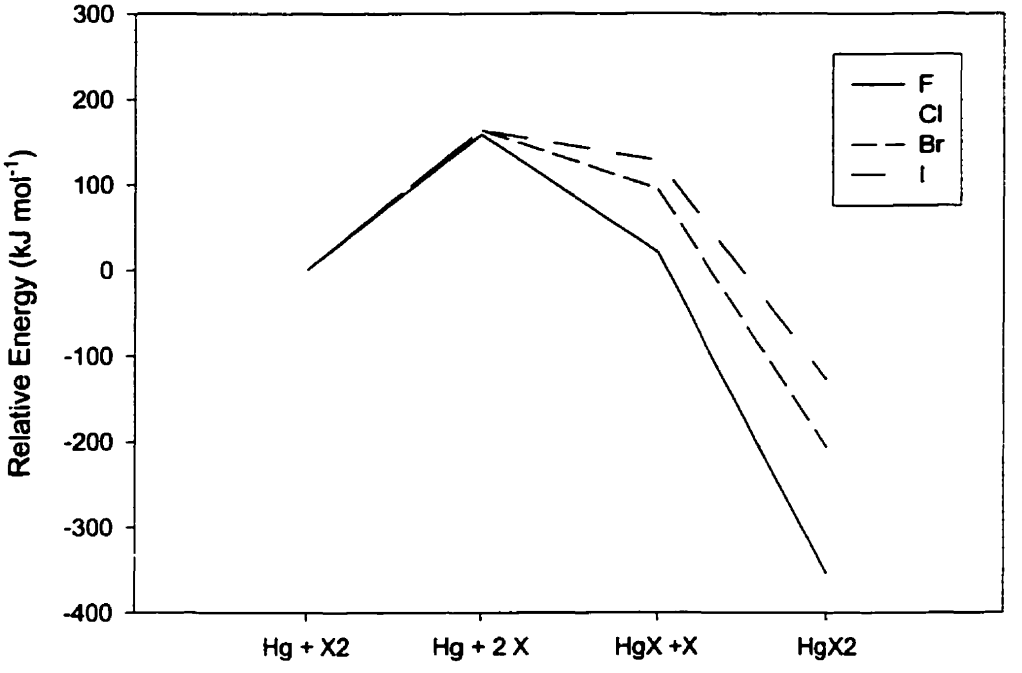

Comparison of Plots 3.2, 3.3, and 3.4 shows that both B3LYP/LanL2DZ and PW91/LanL2DZ represent the enthalpy of formation of the gaseous HgX_2 species from $Hg_{(g)}$ and $2X_{(g)}$ quite well. It is also evident that the enthalpies of reaction for formation of the radical species $HgX_{(g)}$ and the dissociation of $X_{2(g)}$ are both better reproduced by PW91/LanL2DZ than by B3LYP/LanL2DZ. As is seen, there seems to be an over-stabilisation of the radicals in the B3LYP method as compared to PW91 and experiment, whereas the latter method is able to almost exactly replicate the experimental results.

Though the use of these methods was satisfactory for the X and X_2 systems, as seen in the next section, their performance with regard to XO systems left much to be desired. As it has been shown earlier that DFT methods work well when characterising halogen oxides, it was believed that a change of basis set might improve the situation. Due to the limitations of working with mercury, it was decided to use the same basis set for mercury, and to use a different basis set {6-311G(d)]} for the halogens. The thermodynamic data obtained is presented in Table 3.3.

Table 3.3: Reaction Enthalpies of reactions of Hg with halogen species.

Reaction	**Reaction Enthalpy ($-\Delta H$/kJ mol^{-1})**	
	B3LYP/LanL2DZ-6-311G(d)	*Experiment*
Hg + F τ HgF	154.08	137.84
Hg +F_2 τ HgF_2	337.16	355.03
HgF + F τ HgF_2	326.34	375.97
Hg + Cl τ HgCl	112.99	104.23
Hg + Cl_2 τ $HgCl_2$	194.91	207.67
HgCl + Cl τ $HgCl_2$	274.71	346.05
Hg + Br τ HgBr	92.28	69.06
Hg + Br_2 τ $HgBr_2$	153.50	146.83
HgBr + Br τ $HgBr_2$	254.38	301.50

It can be seen from the above that the results from the mixed basis sets are closer to the experimental values than those obtained using the uniform basis sets. It can also be seen that there is very little difference in calculated reaction enthalpy upon inclusion of additional d-polarisation functions.

Similar to the analysis performed for the calculations involving a uniform basis set for all elements, the relative energy levels of the various species involved in the Hg + X_2 system are plotted below in Plot 3.5.

Plot 3.5: Comparison of calculated with experimental reaction enthalpies for reactions of mercury involving halogen species.

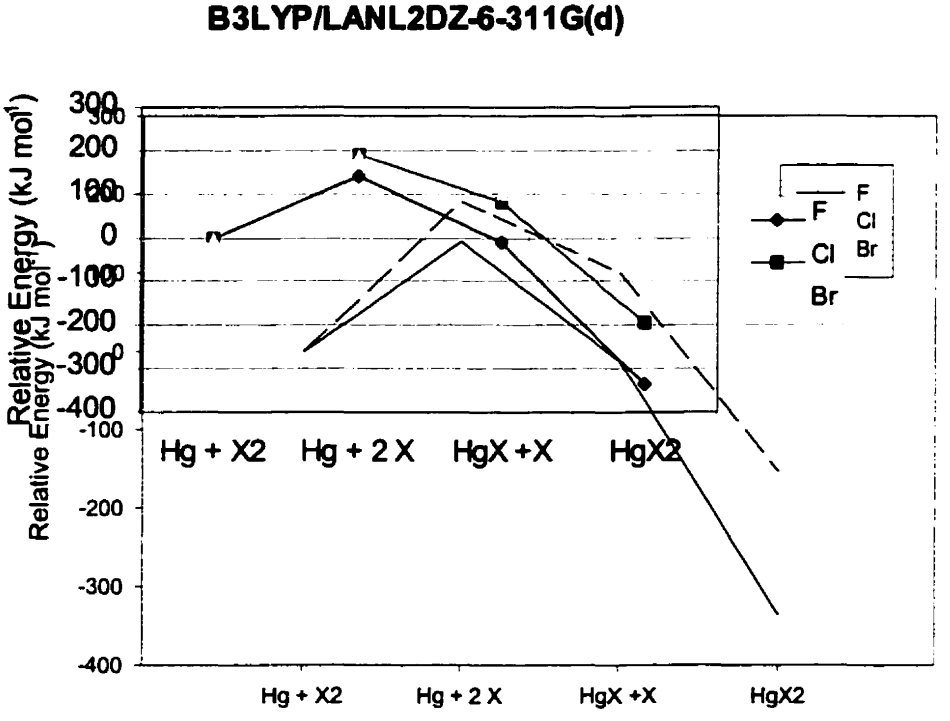

A comparison between Plots 3.5 and 3.4 shows that HgCl is still over-stabilised compared to the experimentally determined values. However, there seems to be no such major discrepancy in the case of F or Br. It is noteworthy that though the experimental reaction enthalpy of HgF + F is expected to be slightly endothermic with respect to Hg + F_2, the calculated reaction enthalpy seems to lie in the slightly negative direction. This is in fact closer than the predictions made with the uniform basis set. Further studies were

also carried out with a second set of d-polarisation functions, and then with one set of f-polarisation functions. The results of the thermodynamic analysis using these modified basis sets are presented below in Table 3.4.

Table 3.4: Reaction Enthalpies of reactions of Hg with halogen species calculated using the B3LYP functional.

Reaction	**Reaction Enthalpy (-ΔH/kJ mol^{-1})**		
	LanL2DZ-6-311G(2d)	*LanL2DZ-6-311G(2df)*	*Experiment*
Hg + F τ HgF	157.21	155.58	137.84
Hg +F_2 τ HgF_2	335.20	328.68	355.03
HgF + F τ HgF_2	337.23	335.87	375.97
Hg + Cl τ HgCl	116.30	114.85	104.23
Hg + Cl_2 τ $HgCl_2$	181.24	173.14	207.67
HgCl + Cl τ $HgCl_2$	283.22	284.22	346.05
Hg + Br τ HgBr	93.75	92.72	69.06
Hg + Br_2 τ $HgBr_2$	154.35	146.14	146.83
HgBr + Br τ $HgBr_2$	256.40	258.44	301.50

The correlation between the calculated values presented above and the experimental values is presented below in Plot 7 along with a comparison with the earlier plots.

Plot 3.6: Comparison of calculated with experimental reaction enthalpies for reactions of mercury involving halogen species.

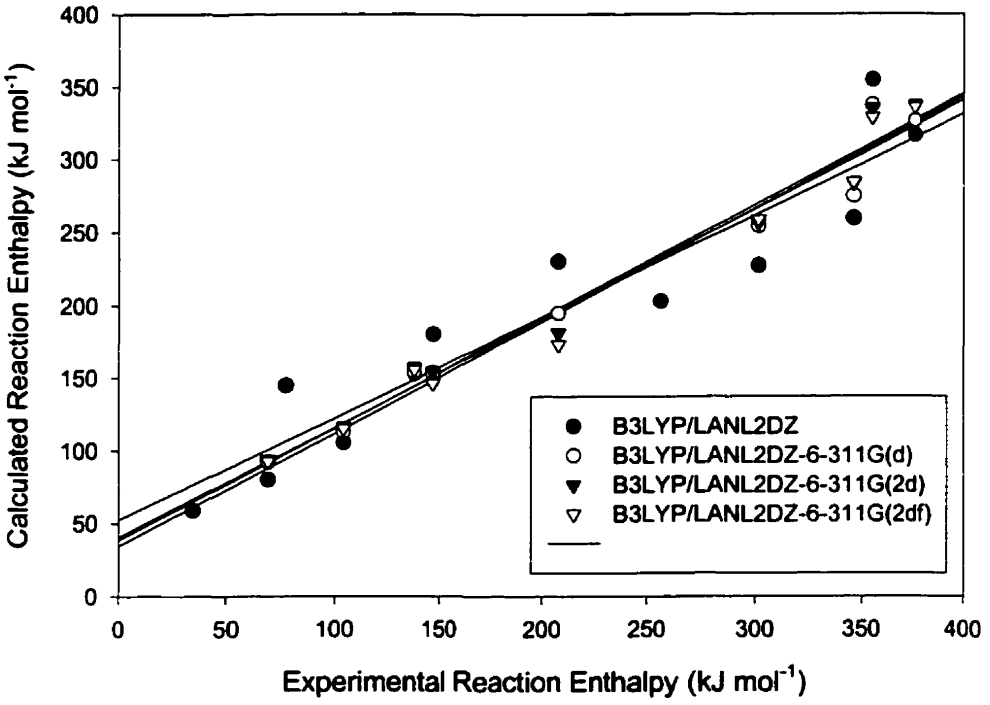

It is seen from Plot 3.6 that the results as obtained from B3LYP calculations with f-type polarisation are similar to those obtained without the addition of such functions to the basis set. It is also seen that the slope of the plot of data including these functions is closer to unity than that without f-polarisation. Hence, there is a slight improvement with increasing complexity of the basis set. This is expected, as the more detailed basis sets are closer to the ideal of the "complete basis set". However, the complete basis set cannot be achieved as the mercury atom is described by an effective core potential for all but the valence and 5d electrons. As a result, there is a limit to the extent to which

agreement exists between the reaction enthalpies obtained by calculations and from experiment. Increasing the extent of description of the mercury atom could of course reduce this discrepancy. This would be at the expense of computational time, as the time scales as at least N^4, where N is the number of basis functions in the system.[54]

In order to better describe the mercury atom, it was decided that f-type polarisation be added. These functions were developed by Hoellwarth and co-workers for p-block and Group II B elements.[55,56] These modified basis sets will hereafter be referred to as LanL2DZ(f) in the remainder of this work, specifying that the f-polarisation has been added to mercury in addition to the standard ECP basis set of Hay and Wadt.[42] As it was determined above that the results are best in the cases when 2d and 2df polarisation functions are applied to the halogens, it was decided that it is only necessary to perform calculations on these systems with application of f-functions to mercury.

3.3.2 XO Species

Similar calculations to those mentioned earlier in the case of X_n species were carried out on systems involving mercury and oxy-halogen compounds, the latter group being a family of compounds of great atmospheric importance. It is known that calculation of halogen oxide species is non-trivial. There are many instances in which even very high-level post-Hartree-Fock methods have failed drastically.[57] Lee and co-workers have shown that the force constant varies with X-O separation in Cl-O and Br-O in an unusual manner. It was however noticed that the behaviour in Cl=O and Br=O was of a more typical nature and approximately linear. The difference is attributed to the loss

of halogen lone pair electrons for the multiply bonded species. These lone pair electrons significantly complicate XO bonds due to through space (electrostatic and dispersion) interactions with the rest of the molecule.[58] It has recently been shown using calculations on XO_2 molecules (X = F, Cl, Br) that DFT calculations can yield accurate geometries and frequencies for halogen oxides and ions. In particular, the B3LYP functional combined with a 6-311G$^+$(2df) basis set generally predicts geometries as accurately as QCISD, yielding slightly larger errors in harmonic vibrational frequencies. In general, DFT methods produce fewer examples of pathological behaviour than single-reference high-level *ab initio* techniques when applied to halogen oxides. Only when a high-spin contamination is present do DFT methods become unreliable in reference to these systems.[57]

The performance of halogen oxides with the systems employed in this study was evaluated in a manner similar to that of the halogen species. The data was compared to data available from NIST of enthalpies of formation. This information was then used to calculate and then tabulate the reaction enthalpies for various reactions. It is to be noted that thermodynamic data is at present only available for FO and ClO. Hence, only these species are used in the comparison with experimental data. The data generated for the oxides of the higher halogens is to be treated as an estimate, which may be subject to revision as and when better experimental data is available. It is also to be noted that the HgOX species mentioned are yet to be observed experimentally, and hence are at the moment hypothetical. It is thought that this might be an intermediate leading to the formation of one or other of the products as per the following scheme:

$$Hg_{(g)} + XO_{(g)} \tau HgOX_{(g)} \tau HgO_{(g)} + X_{(g)} \quad (3.2a)$$

$$\tau HgX_{(g)} + O_{(g)} \quad (3.2b)$$

Table 3.5: Reaction Enthalpies of reactions of Hg with oxy-halogen species.

Reaction	**Reaction Enthalpy (-ΔH/kJ mol^{-1})**		
	B3LYP/LanL2DZ	*PW91/LanL2DZ*	*Experiment*
Hg + FO τ HgOF	49.08	70.67	
Hg +FO τ HgF + O	-285.23	-131.51	-81.94
Hg + FO τ HgO + F	-197.03	-214.69	48.93
Hg + ClO τ HgOCl	13.87	70.16	
Hg + ClO τ HgCl + O	-313.98	-160.88	-165.02
Hg + ClO τ HgO + Cl	-178.31	-182.45	-0.54
Hg + BrO τ HgOBr	46.28	51.77	
Hg + BrO τ HgBr + O	-339.90	-186.68	-355.93
Hg + BrO τ HgO +Br	-178.91	-181.20	33.45
Hg + IO τ HgOI	44.60	65.68	
Hg + IO τ HgI + O	-370.25	-214.87	
Hg + IO τ HgO + I	-188.04	-186.64	

The data above is presented in Plots 3.7 and 3.8 below.

Plot 3.7: Relative energy levels of Hg + XO τ HgOX τ HgO + X τ HgX + O normalised relative to Hg + XO at the B3LYP/LanL2DZ level of theory.

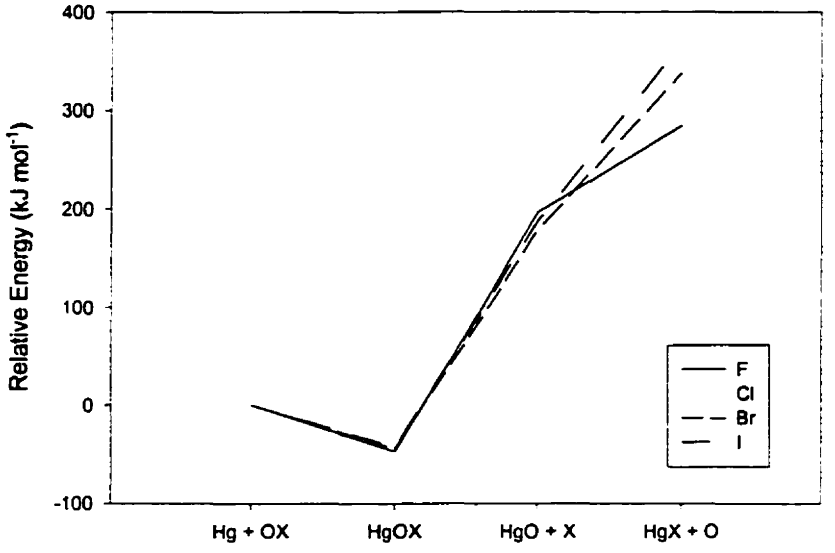

Plot 3.8: Relative energy levels of Hg + XO τ HgOX τ HgO + X τ HgX + O normalised relative to Hg + XO at the PW91/LanL2DZ level of theory.

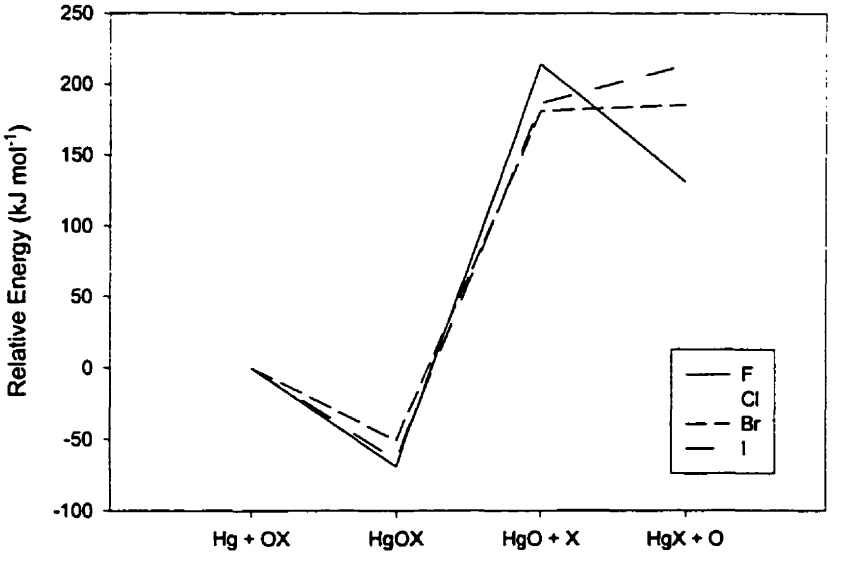

It is seen from the previous two plots that the hypothetical HgOX complex is predicted to be more stable than the separate Hg and XO species. Interestingly, the formation of HgO and HgX are predicted to be endothermic processes and hence are likely to be disfavoured. The prediction of HgO formation being endothermic is contrary to experimental evidence available (Plot 3.9). A comparison of the calculated reaction enthalpies against the experimental values is plotted below in Plot 3.10.

Plot 3.9: Relative energy levels of Hg + XO τ HgOX τ HgO + X τ HgX + O normalised relative to Hg + XO from experimental data.

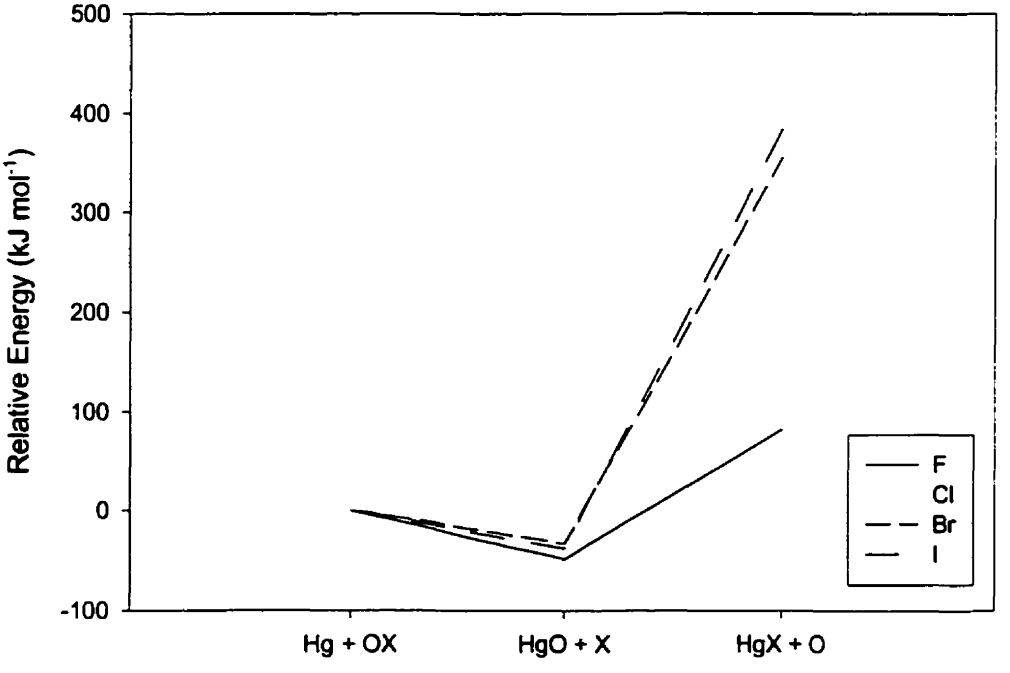

Plot 3.10: Comparison of calculated with experimental reaction enthalpies.

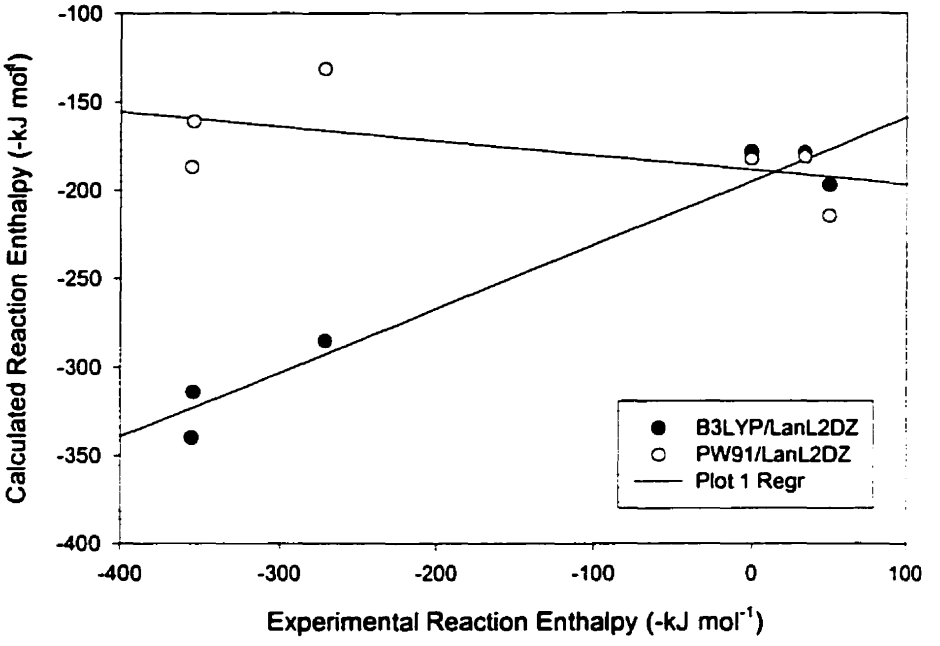

As can be seen above, the calculated reaction enthalpy shows a negative correlation with the experimental value in the case of the PW91 functional. As it has been shown earlier that DFT methods work well when characterising halogen oxides, it was believed that a change of basis set might improve the situation. Due to the limitations of working with mercury, it was decided to use the same basis set for mercury, and to use a different basis set {6-311G(d)} for the halogens and oxygen. In the previous calculations, the atomic oxygen specified is in the singlet state as it is thought that this is the preferred species to emerge from the reaction, and the singlet oxygen (O^1D) is used in all calculations. The enthalpy of formation of $O(^1D)$ is obtained from

the work of Brownsword *et al.* [59] as this data was unavailable from NIST. The thermodynamic data obtained is presented in Table 3.6.

Table 3.6: Reaction Enthalpies of reactions of Hg with oxy-halogen species.

Reaction	**Reaction Enthalpy ($-\Delta H$/kJ mol^{-1})**	
	B3LYP/LanL2DZ-6-311G(d)	*Experiment*
Hg + FO τ HgOF	33.53	
Hg +FO τ HgF + O	-334.29	-271.66
Hg + FO τ HgO + F	-242.27	48.93
Hg + ClO τ HgOCl	3.05	
Hg + ClO τ HgCl + O	-384.79	-354.75
Hg + ClO τ HgO + Cl	-251.68	-0.54
Hg + BrO τ HgOBr	30.67	
Hg + BrO τ HgBr + O	-396.52	-355.93
Hg + BrO τ HgO +Br	-242.69	33.45

It can be seen from the above that the results from the mixed basis sets are closer to the experimental values than those obtained using the uniform basis sets. It is conceivable, then, that by improving the definition of the halogens, more precision can be obtained.

As can be seen from the previous, the correlation between the calculated reaction enthalpies and those from experiment is very good when halogen oxides are considered. The slope between the calculated and experimental reaction enthalpies is calculated to be only ~0.34. This lends credence to the thought that extension of the basis set for the halogens and oxygen may lead to a better representation of the mercury-halogen oxide system. An improved description of the halogen and oxygen atoms is expected to

improve the correspondence between the experimental and calculated reaction enthalpies. In order to observe the difference, calculations were carried out by adding a second d-polarisation function and later by adding an f-polarisation function. The results are presented below in Table 3.7.

Table 3.7: Reaction Enthalpies of reactions of Hg with oxy-halogen species with the B3LYP functional.

Reaction	**Reaction Enthalpy (-ΔH/kJ mol^{-1})**		
	LanL2DZ-6-311G(2d)	*LanL2DZ-6-311G(2df)*	*Experiment*
Hg + FO τ HgOF	31.73	30.23	
Hg +FO τ HgF + O	-344.55	-350.54	-271.66
Hg + FO τ HgO + F	-249.25	-253.43	48.93
Hg + ClO τ HgOCl	26.08	23.81	
Hg + ClO τ HgCl + O	-404.80	-416.49	-354.75
Hg + ClO τ HgO + Cl	-268.59	-278.65	-0.54
Hg + BrO τ HgOBr	26.66	24.62	
Hg + BrO τ HgBr + O	-412.89	-423.34	-355.93
Hg + BrO τ HgO +Br	-254.14	-263.37	33.45

The above data is presented below in Plot 3.11 along with previously obtained data for this system.

Plot 3.11: Comparison of calculated with experimental reaction enthalpies for reactions of mercury involving oxy-halogen (XO) species.

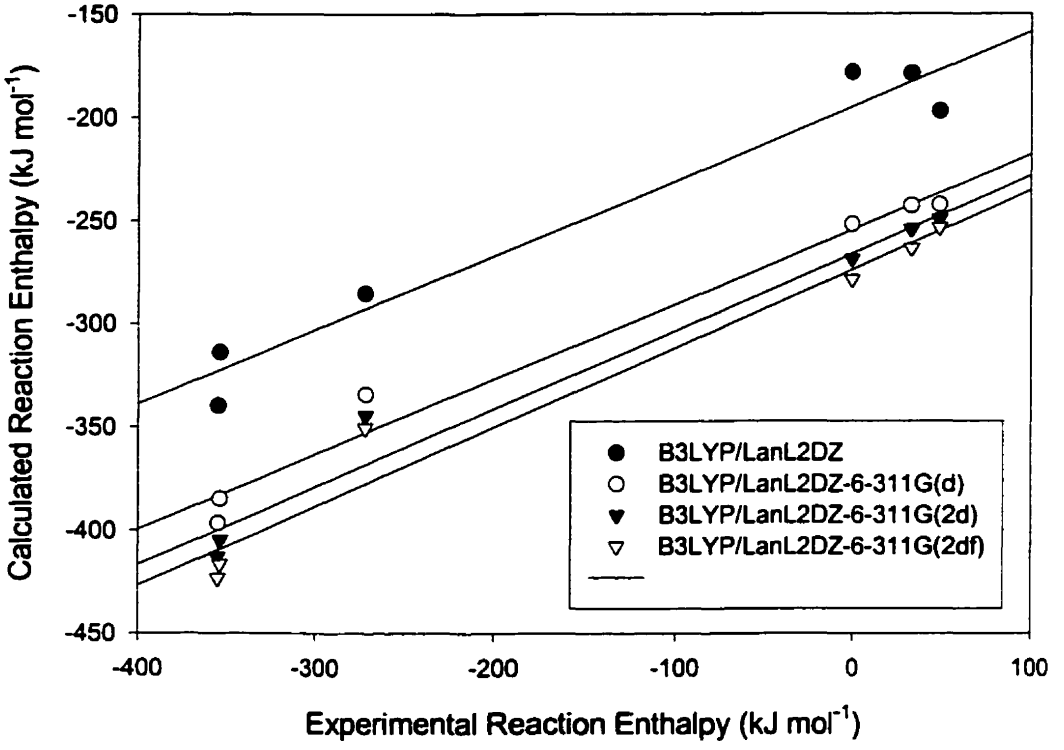

A comparison between Plots 3.11 and 3.10 shows an improvement in the correspondence between experimental and calculated reaction enthalpies for the oxy-halogen systems on increasing the polarisation of the basis functions. It is seen visually however that the points involving the formation of HgX (X = F, Cl) on their own have a slope higher than that of the aggregate plot and that those representing the formation of HgO have a lower slope. This could imply that the source of the problem might be the description of HgO and less a problem of oxy-halogen description. This would imply that the basis set on mercury (LanL2DZ) is inadequate, especially with regard to its

interaction with oxygen. This situation would necessitate the augmentation of the basis set with polarisation functions or changing the ECP.

3.3.3 HgO

The description of reactions involving HgO is concerning due to the very large deviations from experiment observed for the same. It is observed that HgO is predicted to be less stable than it actually is to the tune of over 200 kJ mol^{-1} (Table 3.8 below).

Table 3.8: Stability of HgO relative to Hg and $O(^1D)$.

Basis Set / Method	*B3LYP*	*PW91*	*Other Sources*
LanL2DZ	-238.0	-105.8	
LanL2DZ+6-311G(d)	-243.0	-107.6	
LanL2DZ+6-311G(2d)	-249.3	-113.1	
LanL2DZ+6-311G(2df)	-249.5	-111.5	
LanL2DZ(f)+6-311G(d)	-248.1	-113.1	
LanL2DZ(f)+6-311G(2df)	-257.7	-117.5	
Experiment [27]			-458.4
Experiment [27,60]			-452.2
Previous Calculations [45]			-166.3

This system is thought to be better described as a tetramer cluster of the diatomic oxide, leading to an 8-atom system. This was considered as it has been suggested that MO (M = Zn, Hg) exist as tetramers in the gas phase, [61] in contrast to mass-spectrometry studies exhibiting the presence of MO (M = Zn, Cd, Hg) monomers in the gas phase.[62] It is to be noted that the m/z range studied was not high enough to include the tetramer, and hence the presence of this species may have been missed. Preliminary calculations on the tetramer improve the atomisation energy to within 20 kJ mol^{-1} from the above

deviations of nearly 200 kJ mol^{-1}, suggesting that this may be at least a partial explanation of the observed anomaly. As noted earlier, it is possible that $HgO_{(g)}$ could exist as a tetramer, though this line of reasoning is not completely convincing. The presence of HgO monomers in the gas phase [62] does not permit all of the $HgO_{(g)}$ to exist as tetramers. It is suspected that in fact, $HgO_{(g)}$ does exist largely as a monomer, and that the discrepancy between calculated and experimental enthalpies of formation may be due to the fact that Hg is described by an ECP. It is known that the use of an ECP is untenable in systems wherein the ECP overlaps with bonding and second atom core electrons.[42] This could also explain why HgF and HgF_2 show much greater deviations than the $HgCl_n$ species, though the effect is smaller than for HgO. The similarity in behaviour could well be due to the similar bond lengths in HgO (~2.00 Ⓘ), HgF (~2.15 Ⓘ), and HgF_2 (~2.05 Ⓘ). These short bond lengths could explain the deviation of the calculated formation enthalpies from experiment, if the Hg ECP extends into the bonding and core regions. An analysis of the core potential on Hg at different distances from the nucleus was carried out. It was found that the potential due to core (non-valence shell) electrons is significant for distances as great as 2.5 Ⓘ. The potential at 2.0 Ⓘ (HgO and HgF_2 equilibrium inter-atomic distances) is nearly 1.7 au. The potential at the HgF inter-atomic distance is still in excess of 1.0 au. This implies that the second nucleus is lying within the potential simulating the core electrons. In effect, the bonding (or valence) wavefunctions do not extend out as far from the nucleus as the core electrons are presumed to. This can be solved by the development and use of a well-constructed high-quality all-electron basis set for Hg, which is beyond the scope of this study.

The effect of the overlap between the ECP and valence (and bonding) electrons was studied for the HgO system using an all-electron basis set prepared by Gleichmann and Hess.[63] Calculations were performed only for this system as the large number of electrons (88) and basis functions (194, with 635 gaussians) makes the application to other systems prohibitively time-consuming. Hence, this basis set was used only to quantify the contribution of the ECP to the deviation from experiment. The results of these calculations are presented below in Table 3.9.

Table 3.9: Stability of HgO relative to Hg and O(^{1}D) when employing Gleichmann-Hess (GH) basis set[63] for Hg.

Method	**Enthalpy (kJ mol^{-1})**	**Enthalpy Deviation (kJ mol^{-1})**
B3LYP/LanL2DZ+6-311G(2d)	-249.3	209.1
B3LYP/GH+6-311G(2d)	-324.3	134.1
PW91/LanL2DZ+6-311G(2d)	-113.1	345.3
PW91/GH+6-311G(2d)	-202.7	255.8

As can be seen from the above table, there is a significant improvement (60-80 kJ mol^{-1}) in the reaction enthalpy for the formation of HgO upon utilisation of the GH basis set as compared to the LanL2DZ basis set. However, calculation using this basis set at the HF level of theory only yields a first ionisation potential of 7.10 eV for Hg^0 as compared to the known value of 10.437 eV [3]. The first ionisation energy was calculated to be 8.53 eV using the PW91 functionals on the GH basis set.

CHAPTER IV: Kinetic Treatment and Reaction Rate Evaluation

4.1 Introduction

The speciation of oxidised mercury in the atmosphere depends to a large extent on the thermodynamics of the system. It is however important to note that a strongly thermodynamically favoured reaction would only be important if it is fast enough to be observed. Hence, the importance of the investigation into the kinetics of the various mercury-halogen reactions outlined in the previous chapter. It is expected that these will assist in the evaluation of the relative importance to be attached to the various available pathways. One can easily see that the relative velocity of a pathway depends on the rate constant and (in most cases) the concentration (or number density) of the oxidant.

4.1.1 Transition State Approach

Boltzmann averaging of the reactive flux over the initial states and the collision energy can be used to rigorously calculate the exact thermal rate constant for an elementary bimolecular reaction A + B τ P.

$$k = \langle \sigma v \rangle$$

$$= 4\pi/Q_{int} \, \Sigma_{fi} \exp(-\varepsilon_i/k_B T) \, {}^{\circ}{}_0^{\blacksquare}(\mu/2\pi k_B T)^{3/2} v_i^3 \exp(-\mu v_i^2/2k_B T)\sigma_{fi}(v_i) \, dv_I \qquad (4.1)$$

where μ is the translational mass, ε_i is the eigenenergy of the internal state of the colliding partners, and v_i is the relative speed of the collision. The quantum partition function Q_{int} is defined as

$$Q_{int} = \Sigma_i \exp(-\varepsilon_i/k_B T) \qquad (4.2)$$

where the summation is over all energetically accessible internal states of the reactants. The reaction cross-section σ_{fi} is given by

$$\sigma_{fi} = \pi''^2/\mu^2 v_i^2 \, \Sigma_J (2J+1) \, |S_{fi}^J|^2 \qquad (4.3)$$

where S_{fi}^J is the state-to-state reactive matrix element. The rate equation produced above can then be rearranged using the above definitions to yield

$$k = k_B T/2\pi'' Q_0 \, {}^{\circ}{}_0^{\blacksquare} \, N(E) \exp(-E/k_B T) \, / \, k_B T \, De \qquad (4.4)$$

where Q_0 is the total partition function for the reactants A+B.

$$Q_0 = Q_{int} (2\pi\mu k_B T/\hbar^2)^{3/2}$$
$$= Q_{int} Q_{trans}$$
$$= Q_A Q_B \quad (4.5)$$

N(E) is the cumulative reaction probability and is defined as the sum over both initial and final states of reaction probability.

$$N(E) = \Sigma_J (2J + 1) \Sigma_{fi} |S_{fi}^J|^2 \quad (4.6)$$

Performing a partial integration on Eq. (4.4) yields the form

$$k = k_B T/hQ_A Q_B \int_0^\infty \rho(E) \exp(-E/k_B T)\, dE \quad (4.7)$$

where

$$\rho(E) = dN(E)/dE \quad (4.8)$$

The quantity $\rho(E)$ may be considered to be "density of states" from which can be defined a partition function

$$Q_{ex}^A = \int_0^\infty \exp(-E/k_B T)\, r(E)\, dE$$
$$= (1/k_B T) \int_0^\infty \exp(-E/k_B T)\, N(E)\, dE \quad (4.9)$$

Thus, the rate equation becomes

$$k = (k_B T/h) (Q_{ex}^A/Q_A Q_B) \quad (4.10)$$

From the expression for the rate constant of a bimolecular reaction, it is a straightforward exercise to derive the rate expression for the unimolecular dissociation to be

$$k(E) = (1/h) (N(E)/\rho(E)) \quad (4.11)$$

A more detailed treatment involving consideration of the vibrational modes of the reactants and transition state, yield the following expression for the reaction rate constant (defining $\beta = 1/k_B T$)

$$k = \kappa^{ex}(T) (k_B T/h) (Q_{tr}^A Q_{vib}^A/Q_{tr}^A Q_{vib}^A Q_{tr}^B Q_{vib}^B) \exp(-\beta E_0^b) \quad (4.12)$$

where

$$Q_{vib}^A = \Sigma_n \exp(-\beta E_n'^b) \quad (4.13)$$

is a partition function involving the internal energies measured at the position of the barrier along the reaction co-ordinate. The expression $E_n'^b$ is the difference between the

activation barriers for state n and state 0, whereas E_n^b is the vibrational energy of state n. The transmission factor κ^{ex} is given by

$$\kappa^{ex}(T) = (1/Q_{vib}^A) \Sigma_n \exp(-\beta E_n^{'b}) P_n^r(T)/P_n^{cl}(T) \quad (4.14)$$

The Boltzmann averaged classical probability is given by

$$P_n^{cl}(T) = \exp(-\beta E_n^b) \quad (4.15)$$

The average probability of reactant molecules in state n is given by

$$P_n^r(T) = {}^{\circ} d(E_{kin}\beta) \exp(-E_{kin}\beta) P_n^r(v) \quad (4.16)$$

where E_{kin} is the kinetic energy and $P_n^r(v)$ is the reaction probability for reactant molecules in a specific vibrational quantum state n. [29]

4.1.2 Computational Details

Kinetic analysis was carried out using the Classical Transition State Theory. It was noticed that in the case of some sets of reactants, many sets of products could be formed, each set of products formed through a unique activation complex. The products formed from the activated complex are determined by the negative eigenvector of the latter. Some activated complexes had complex negative eigenvectors. In those cases, an intrinsic reaction co-ordinate (IRC) calculation was performed to determine the reactants and products connected by the transition state. The reaction rate constant for these systems was calculated by

$$k = (k_B T/h) (Q^A/Q^A Q^B) \exp(-\beta E_0^b) \quad (4.17)$$

The partition functions are obtained from the thermodynamic evaluation procedure.

It was noticed that some reactions, such as the addition of halogen atoms (radicals) to Hg occurred without any activation barrier. In such cases, the dissociation was treated as by Holbrook *et al.* [30] As per this treatment, the high-pressure limit for the rate of unimolecular decomposition (k_∞) of a diatomic species is given by

$$k_\infty = \nu \exp(-D_0/k_B T) \quad (4.18)$$

where ν is the vibrational frequency and D_0 is the ground state dissociation energy. The dissociation energy is taken as the difference between the energy of the bound diatomic and the free atoms. The equilibrium constant between the dissociated and associated species can then be defined as

$$K_{eq} = k_{=} / k_{Ass} \quad (4.19)$$

where k_{Ass} is the rate constant for the association reaction, which is of interest. The equilibrium constant as written depends on the free energy of dissociation as

$$K_{eq} = \exp(-\Delta_{Diss}G/RT) \quad (4.20)$$

Hence, the rate of the associative pathway is

$$k_{Ass} = \nu \exp(-N_A D_0/RT) \exp(\Delta_{Diss}G/RT) \quad (4.21)$$

4.2 Results and Discussion

Calculation of the reaction rate constant requires that the transition state structure be determined. In order to calculate the transition states, proper selection of methods and basis sets is necessary. A comparison was made of the reaction enthalpy deviations for the various reactions considered in the previous chapter. Reaction rates were only calculated using the LanL2DZ and LanL2DZ(f)|6-311G(2df) with both sets of functionals, as a comparison between the simplest and most extended cases. The temperature in the Arctic regions (the area of interest for this study) is known to drop to around 233 ! 10 K.[64-66] To cover the range of temperatures observed, the reaction rate constants were evaluated at 298 K and 238 K.

4.2.1 Barrierless Reactions

There were a number of reactions in this study which proceeded without passing over an activation barrier. These reactions were broadly: (i) the addition of halogens (X/X_2) to mercury (ii) the radical combination of mercury halides with radical halogens. The reaction rate constants for the reactions in which there was no activation barrier were

calculated as detailed above. The results of the calculations are outlined below in Table 4.1. The uncertainty range is reported at the 95 % confidence level.

Table 4.1: Reaction Rates at 298 K, 1 bar for addition reactions of halogens to mercury without an activation barrier.

Reaction	**Rate Constant k (cm^3 $molec^{-1}$ s^{-1})**				
	Method A	*Method B*	*Method C*	*Method D*	*Mean*
Hg + F τ HgF	5.36×10^{-12}	5.28×10^{-12}	5.36×10^{-12}	5.35×10^{-12}	(5.3 ! 0.1) x 10^{-12}
HgF + F τ HgF_2	9.49×10^{-15}	1.08×10^{-14}	1.19×10^{-14}	1.30×10^{-14}	(1.1 ! 0.5) x 10^{-14}
Hg + Cl τ HgCl	4.64×10^{-12}	4.45×10^{-12}	4.67×10^{-12}	4.50×10^{-12}	(4.6 ! 0.3) x 10^{-12}
HgCl + Cl τ $HgCl_2$	3.89×10^{-15}	4.19×10^{-15}	4.14×10^{-15}	4.14×10^{-15}	(4.1 ! 0.4) x 10^{-15}
Hg + Br τ HgBr	3.49×10^{-12}	3.32×10^{-12}	3.49×10^{-12}	3.34×10^{-12}	(3.4 ! 0.3) x 10^{-12}
HgBr + Br τ $HgBr_2$	2.15×10^{-15}	2.51×10^{-15}	2.39×10^{-15}	2.10×10^{-15}	(2.3 ! 0.6) x 10^{-15}

N.B.:

Method A: B3LYP/LanL2DZ

Method B: B3LYP/LanL2DZ(f)-6-311G(2df)

Method C: PW91/LanL2DZ

Method D: PW91/LanL2DZ(f)-6-311G(2df)

From the above, it can be seen that for similar reactions, the reaction rate decreases when going down the group. The reaction rates for these reactions are seen to differ by less than an order of magnitude when going from F to Br. This is an expected trend as the higher halogens are in general more reactive than the lower halogens. The effect of mass is also seen in this trend. It is also significant that all four method-basis set combinations yield very similar values for the rate constant. The relative uncertainties are observed to be in the region of 10 % on most of the systems presented above. The temperature in the Arctic regions (the area of interest for this study) is known to drop to very low temperatures, and hence the rate constants were also evaluated for these

reactions at 238 K, in order to see the effect of temperature. These results are tabulated below in Table 4.2.

Table 4.2: Reaction Rates at 238 K, 1 bar for addition reactions of halogens to mercury without an activation barrier.

Reaction	**Rate Constant k (cm^3 $molec^{-1}$ s^{-1})**				
	Method A	*Method B*	*Method C*	*Method D*	*Mean*
Hg + F τ HgF	4.1×10^{-12}	4.1×10^{-12}	7.1×10^{-12}	7.1×10^{-12}	$(6 \pm 6) \times 10^{-12}$
HgF + F τ HgF_2	1.2×10^{-14}	6.1×10^{-15}	1.5×10^{-14}	1.4×10^{-14}	$(1 \pm 1) \times 10^{-14}$
Hg + Cl τ HgCl	1.8×10^{-12}	5.4×10^{-12}	5.6×10^{-12}	5.4×10^{-12}	$(5 \pm 6) \times 10^{-12}$
HgCl + Cl τ $HgCl_2$	1.1×10^{-17}	2.0×10^{-20}	4.6×10^{-15}	4.3×10^{-15}	$(3 \pm 8) \times 10^{-15}$
Hg + Br τ HgBr	3.3×10^{-12}	3.8×10^{-12}	4.0×10^{-12}	3.8×10^{-12}	$(4 \pm 1) \times 10^{-12}$
HgBr + Br τ $HgBr_2$	5.0×10^{-16}	8.0×10^{-21}	2.4×10^{-15}	2.0×10^{-15}	$(1 \pm 4) \times 10^{-15}$

N.B.:

Method A: B3LYP/LanL2DZ

Method B: B3LYP/LanL2DZ(f)-6-311G(2df)

Method C: PW91/LanL2DZ

Method D: PW91/LanL2DZ(f)-6-311G(2df)

All of the four combinations of method and basis set considered yield very similar values for the rate constant. It can also be seen that the reaction rates calculated at the B3LYP level were consistently lower than those calculated at the PW91 level of theory, the latter two agreeing well with each other.

4.2.2 Reactions passing through an Activation Barrier

Most of the reactions studied pass through an activated complex. This enables direct use of the Classical Transition State Theory. It was noticed that many transition states obtained with limited basis set (ECP) disappeared upon use of more extended basis sets. This could suggest that these are imaginary transition states which are the result of

mathematical accidents. The results obtained are tabulated below in Table 4.3. The volume correction term RT/P_0 in which the temperature and pressure dependent terms are present has not been included in the pre-exponential factor. This explicitly temperature dependent term must therefore be multiplied to the Arrhenius factor before the final rate constant is obtained at a given temperature and pressure. An explicit evaluation of the above yields the reaction rate constant (for bimolecular reactions) in SI units, or $M^{-1}s^{-1}$. Conversion to molecular units (cm^3 $molec^{-1}$ s^{-1}), as is commonly used in atmospheric studies, is accomplished by division by N_A x 1000 cm^3 L^{-1} where N_A is the Avogadro constant. The reaction rate constant is hence given by

$$k = A\,(RT/P_0)\,(1000\,N_A\,cm^3\,L^{-1})\,\exp(-E_a/RT) \qquad (4.22)$$

Comparison of Equations 4.22 and 4.17 shows that

$$A = (k_B T/h)\,(Q^A/Q^A Q^B) \qquad (4.23)$$

and this value is seen to be independent of temperature when evaluated over a narrow range of temperatures.

Table 4.3: Reaction rate parameters for reactions involving an explicit transition state.

Reaction	**Pre-exponential Factor A (s^{-1})**	**Activation Energy E_a (kJ mol^{-1})**
Hg + FO τ HgF + O(^{1}D)	(1.1 ! 2) x 10^8	-5 ! 400
Hg + FO τ HgO + F	(1.2 ! 2) x 10^8	160 ! 300
Hg + FO τ HgOF	(1.1 ! 5) x 10^8	250 ! 400
Hg + ClO τ HgCl + O(^{1}D)	(6.7 ! 8) x 10^9	130 ! 200
Hg + ClO τ HgO + Cl	(3.5 ! 3) x 10^9	420 ! 300
Hg + ClO τ HgOCl	(3.5 ! 2) x 10^9	69 ! 30
Hg + BrO τ HgBr + O(^{1}D)	(6.7 ! 6) x 10^7	-5.6 ! 4
Hg + BrO τ HgO + Br	(1.1 ! 2) x 10^{10}	130 ! 200

It can be seen from the above that there are some reactions which seem to have negative activation energies. This is likely an aberration as the uncertainties in energy calculations are typically of the order of 5 kJ mol^{-1}. Hence, it is likely that the transition state may be approximately thermo-neutral relative to the reactants. It can also be seen that for similar reactions (in which only the halogen atom is substituted), the reaction rate at 298 K decreases as one proceeds down the group. This is evident from the fact that the activation energy increases in the said direction, with a concomitant decrease in the Arrhenius pre-exponential factor. The transition state energies of Hg + XO reactions are very uncertain due to the fact that the transition state geometries exhibit short Hg-O and Hg-X distances. As was explained earlier, the overlap of the ECP with the core electrons of the O and X atoms leads to large deviations from reality. Hence, these values can only be taken as preliminary estimates until a better means of representing these systems is available.

CHAPTER V: Summary

The presence of mercury in a troposphere inhabited by a large number of natural and synthetic compounds, as also radical species and the like presents the possibility of forming oxidised mercury compounds. These compounds can be produced in the gas-phase and in aerosols. This project focussed on the behaviour of mercury in the gas-phase, particularly the interaction with reactive halogen species.

A tentative reaction scheme was devised to determine the products and relative probabilities for the various reactions therein. It was found that the reactions between mercury and halogens (X/X_2) tend to be strongly exothermic in the addition direction. The same was true for reactions in which X was added to HgX to form HgX_2. The formation of HgX and the subsequent addition of a halogen radical to form HgX_2 are families of reactions occurring without passing over an activation barrier. Reaction rates for this family of reactions were calculated by evaluating the dissociation rate and the equilibrium constant between the products and reactants.

The reactions of halogen oxides (XO) with mercury were of greater interest, and also caused the greatest amount of consternation. This was borne out by the fact that reaction enthalpies for these reactions deviated from experimental (where known) enthalpies by an appreciable amount. This was manifest to the greatest extent in the reactions leading to the formation of HgO. This latter set of reactions deviated from experiment by as much as 200 kJ mol^{-1} and decreased with an improvement in the atomic

description of both mercury and the oxy-halogen species. This suggested, and it was later confirmed that this was due to an overlap between the ECP on mercury and the inner electrons on oxygen in HgO. It is known that the use of an ECP is untenable in cases where the ECP overlaps with bonding electrons or non-bonding electrons on other atoms. Similar deviations were also found in the case of HgF and HgF_2 wherein the same reasoning could be applied. It was found that HgO could be better described with an all-electron basis set on Hg, but the improvement was only of the order of 80 kJ mol^{-1}. The remainder could be due to the suggestion that HgO possibly exists as a tetramer in the gas phase, which would affect the experimentally determined formation enthalpy. The complications arising in the case of HgO could play a role in the large (>100 kJ mol^{-1}) activation energies calculated for several of the Hg + XO reactions. It is likely that the true activation energy is much lower, however the precision is highly limited by the overlap between the Hg ECP and the oxygen (or in some cases, halogen) non-bonding electrons.

It is observed that the vast majority of reactions considered in this study are considerably fast, and it is very likely that they play a major role in the chemistry of mercury in the gas phase. It should however be kept in mind that this is a small subset of the possible chemistry that can occur involving mercury in the atmosphere, and there are many gas phase reactions which have not been considered as they are beyond the scope of this study.

CHAPTER VI: Future Directions

6.1 Mixed Halides

The preceding sections detailed the reaction rate analyses for the reactions of gaseous mercury with halogen and halogen oxide species. It may have been noted that reactions leading to the formation of mixed halides had not been considered. This is an important area to look into. It is known that when a mixture of halogens is present, there is the possibility of forming mixed halides of mercury. It is also possible for displacement reactions to occur. The reactions involving the chloro, bromo, and iodo complexes of mercury with halogens to form mixed halides are found to be moderately thermodynamically favoured compared to the presence of the "pure" halides.[67] By analogy with the pure halides, it is expected that the addition of a second halogen atom to a mercury mono-halide radical species would occur without an activation barrier. Such a situation would make these pathways more favoured than the formation of the single-halogen dihalides. This conjecture however needs to be verified before these systems can be treated in the above manner.

6.2 Effect of Oxygen

This study has not looked at the role of oxygen on the many pathways available for the oxidation of mercury. It is conceivable that one or more of the intermediates could interact with an oxygen molecule to change the observed chemistry. Preliminary calculations have shown that the formation of peroxy-compounds of the type $XHgOO^{\bullet}$ is moderately thermodynamically favoured. Further work will therefore be required to

characterise the nature of the chemistry involving the $XHgOO^{\exists}$ species. This line of work is especially important due to the comparatively large concentration of oxygen relative to that of the halogen species. This is likely to affect the product distribution of the deposited mercury.

6.3 Mercury Reduction Pathways in Condensed Phases

The presence of many organic and inorganic reducing agents on the surface and in aqueous systems leads to the possibility for redox couples being set up. The reduction of Hg^{++} to Hg^0 has been observed.[18,68] The photo-reduction of aqueous Hg^{++} is known to be accelerated in the presence of organic acids such as fulvic acid, and alcohols.[69,70] This is bound to affect the overall mercury budget in the atmosphere, which could take the form of either a diffuse surface emission or a re-volatilisation from aerosols.

6.4 Interaction of Mercury Species with Organics

There are a large number of organic species in the lower troposphere. It is therefore possible that there may be interactions between mercury itself or mercury species and some organic molecules or intermediate species. Of particular concern is the formation of methylated mercury species, methane being the most abundant organic species in the atmosphere.

REFERENCES

(1) Nriagu, J. O. "Production and uses of mercury". In *The biogeochemistry of mercury in the environment*; Nriagu, J. O., Ed.; Elsevier/North-Holland Biomedical Press: Amsterdam, **1979**; Vol. 3; pp 23-40.

(2) Stopford, W. "Industrial exposure to mercury". In *The biogeochemistry of mercury in the environment*; Nriagu, J. O., Ed.; Elsevier/North-Holland Biomedical Press: Amsterdam, **1979**; Vol. 3; pp 367-98.

(3) Clark *Clark's Tables: Science Data Book*, Revised Edition (First Published 1904) ed.; Orient Longman Ltd.: , **1992**.

(4) Andren, A. W.; Nriagu, J. O. "The global cycle of mercury". In *The biogeochemistry of mercury in the environment*; Nriagu, J. O., Ed.; Elsevier/North-Holland Biomedical Press: Amsterdam, **1979**; Vol. *3*; pp 1-22.

(5) Matheson, D. H. "Mercury in the atmosphere and in precipitation". In *The biogeochemistry of mercury in the environment*; Nriagu, J. O., Ed.; Elsevier/North-Holland Biomedical Press: Amsterdam, 1979; Vol. 3; pp 113-29.

(6) Carty, A. J.; Malone, S. F. "The chemistry of mercury in biological systems". In *The biogeochemistry of mercury in the environment*; Nriagu, J. O., Ed.; Elsevier/North-Holland Biomedical Press: Amsterdam, **1979**; Vol. 3; pp 433-80.

(7) Schroeder, W. H.; Barrie, L. A. "Is Mercury Input to Polar Ecosystems Enhanced by Springtime Ozone Depletion Chemistry?". In *IGAC Newsletter*, **1998**; pp 7-8.

(8) Hall, B. *Water, Air and Soil Pollution* **1995**, *80*, 301-15.

(9) Schroeder, W. H.; Yarwood, G.; Niki, H. *Water, Air and Soil Pollution* **1991**, ***56***, 653-66.

(10) Lindberg, S. E.; Stratton, W. J. *Environmental Science and Technology* **1998**, ***32***, 49-57.

(11) P'yankov, V. A. *Zhurnal Obschey Khimii (Journal of General Chemistry)* **1949**, ***19***, 224-9.

(12) Iverfeldt, A.; Lindqvist, O. *Atmospheric Environment* **1986**, ***20***, 1567-73.

(13) Lin, C.-J.; Pehkonen, S. O. *Journal of Geophysical Research* **1998**, *103*, 28,093-28,102.

(14) Tokos, J. J. S.; Hall, B.; Calhoun, J. A.; Prestbo, E. M. *Atmospheric Environment* **1998**, ***32***, 823-7.

(15) Yamamoto, M. *Chemosphere* **1996**, ***32***, 1217-24.

(16) Lin, C.-J.; Pehkonen, S. O. *Atmospheric Environment* **1999**, ***33***, 2067-79.

(17) Munthe, J.; Xiao, Z. F.; Lindqvist, O. *Water, Air and Soil Pollution* **1991**, ***56***, 621-30.

(18) Van Loon, L.; Mader, E.; Scott, S. L. *Journal of Physical Chemistry A* **2000**, ***104***, 1621-6.

(19) Granite, E. J.; Pennline, H. W.; Hoffman, J. S. *Industrial & Engineering Chemistry Research* **1999**, ***38***, 5034-7.

(20) Ariya, P. A.; Jobson, B. T.; Sander, R.; Niki, H.; Harris, G. W.; Hopper, J. F.; Anlauf, K. G. *Journal of Geophysical Research* **1998**, ***103***, 13169-80.

(21) Barrie, L.; Platt, U. *Tellus, Series B* **1997**, ***49B***, 450-4.

(22) Langendorfer, U.; Lehrer, E.; Wagenbach, D.; Platt, U. *Journal of Atmospheric Chemistry* **1999**, ***34***, 39-54.

(23) Martinez, M.; Arnold, T.; Perner, D. *Ann. Geophys.* **1999**, ***17***, 941-56.

(24) Mueller, R.; Crutzen, P. J.; Grooss, J.-U.; Bruehl, C.; Russell, J. M., III; Tuck, A. F. *Journal of Geophysical Research* **1996**, ***101***, 12531-54.

(25) Ramacher, B.; Rudolph, J.; Koppmann, R. *Journal of Geophysical Research* **1999**, ***104***, 3633-53.

(26) Frisch, M. J.; Trucks, G. W.; Schlegel, H. B.; Scuseria, G. E.; Robb, M. A.; Cheeseman, J. R.; Zakrzewski, V. G.; Montgomery, J., J. A. ; Stratmann, R. E.; Burant, J. C.; Dapprich, S.; Millam, J. M.; Daniels, A. D.; Kudin, K. N.; Strain, M. C.; Farkas, O.; Tomasi, J.; Barone, V.; Cossi, M.; Cammi, R.; Mennucci, B.; Pomelli, C.; Adamo, C.; Clifford, S.; Ochterski, J.; Petersson, G. A.; Ayala, P. Y.; Cui, Q.; Morokuma, K.; Malick, D. K.; Rabuck, A. D.; Raghavachari, K.; Foresman, J. B.; Cioslowski, J.; Ortiz, J. V.; Baboul, A. G.; Stefanov, B. B.; Liu, G.; Liashenko, A.; Piskorz, P.; Komaromi, I.; Gomperts, R.; Martin, R. L.; Fox, D. J.; Keith, T.; Al-Laham, M. A.; Peng, C. Y.; Nanayakkara, A.; Gonzalez, C.; Challacombe, M.; Gill, P. M. W.; Johnson, B.; Chen, W.; Wong, M. W.; Andres, J. L.; Gonzalez, C.; Head-Gordon, M.; Replogle, E. S.; Pople, J. A. Gaussian 98, Revision A.7; Gaussian, Inc.: Pittsburgh PA,, 1998.

(27) NIST. NIST Chemistry Webbook. In *http://www.webbook.nist.gov/chemistry*, **1998**.

(28) Lide, D. R. CRC Handbook of Chemistry and Physics; 81 ed.; CRC Press:, **2000**.

(29) Billing, G. D.; Mikkelsen, K. V. *"Introduction to Molecular Dynamics and Chemical Kinetics"*; John Wiley and Sons: , **1996**.

(30) Holbrook, K. A.; Pilling, M. J.; Robertson, S. H. *"Unimolecular Reactions"*; John Wiley and Sons: , 1996.

(31) Hohenberg, P.; Kohn, W. *Physical Review* **1964**, ***136***, B 864-B 71.

(32) Laird, B. B.; Ross, R. B.; Ziegler, T. "Density-Functional Methods in Chemistry: An Overview". In *Chemical Applications of Density Functional Theory*; Laird, B. B., Ross, R. B., Ziegler, T., Eds.; American Chemical Society:, **1995**; pp 1-19.

(33) Kohn, W.; Sham, I. J. *Physical Review* **1965**, ***140***, A 1133.

(34) Baerends, E. J.; Gritsenko, O. V.; van Leeuwen, R. "Effective One-Electron Potential in the Kohn-Sham Molecular Orbital Theory". In *Chemical Applications of Density Functional Theory*; Laird, B. B., Ross, R. B., Ziegler, T., Eds.; American Chemical Society:, **1995**; pp 20-41.

(35) Becke, A. D. *Journal of Chemical Physics* **1993**, ***98***, 5648-52.

(36) Vosko, S. H.; Wilk, L.; Nusair, M. *Canadian Journal of Physics* **1980**, ***58***, 1200.

(37) Lee, C.; Yang, W.; Parr, R. G. *Physical Review B* **1988**, ***37***, 785.

(38) Frisch, A.; Frisch, M. J. *Gaussian 98 User's Reference*, Second Edition ed.; Gaussian, Inc.: Pittsburgh, USA, **1999**.

(39) Wang, Y.; Perdew, J. P. *Physical Review B* **1991**, ***44***, 13,298-13,307.

(40) Perdew, J. P.; Wang, Y. *Physical Review B* **1992**, ***45***, 13,244-13,9.

(41) Pople, J. A.; Head-Gordon, M. *Journal of Chemical Physics* **1987**, ***87***, 5968-75.

(42) Hay, P. J.; Wadt, W. R. *Journal of Chemical Physics* **1985**, ***82***, 270-83.

(43) Krishnan, R.; Binkley, J. S.; Seeger, R.; Pople, J. A. *Journal of Chemical Physics* **1980**, ***72***, 650-4.

(44) Cundari, T. R.; Yoshikawa, A. *Journal of Computational Chemistry* **1998**, ***19***, 902-11.

(45) Hu, A.; Otto, P.; Ladik, J. *Theochem* **1999**, ***468***, 163-9.

(46) Barone, V.; Bencini, A.; Totti, F.; Uytterhoeven, M. G. *Organometallics* **1996**, ***15***, 1465-9.

(47) Jonas, V.; Thiel, W. *Journal of the Chemical Society, Dalton Transactions* **1999**, 3783-90.

(48) Luna-Garcia, H.; Castillo, S.; Ramirez-Solis, A. *Journal of Chemical Physics* **1999**, ***110***, 11315-22.

(49) Dolg, M.; Flad, H.-J. *Journal of Physical Chemistry* **1996**, ***100***, 6147-51.

(50) Liu, W.; Franke, R.; Dolg, M. *Chemical Physics Letters* **1999**, ***302***, 231-9.

(51) Koper, M. T. M.; van Santen, R. A. *Surface Science* **1999**, ***422***, 118-31.

(52) Lupinetti, A. J.; Jonas, V.; Thiel, W.; Strauss, S. H.; Frenking, G. *Chemistry - A European Journal* **1999**, ***5***, 2573-83.

(53) Liao, M.-S.; Zhang, Q.-E.; Scwarz, W. H. E. *Inorganic Chemistry* **1995**, ***34***, 5597-605.

(54) Jensen, F. *Introduction to Computational Chemistry*; John Wiley & Sons: , 1999.

(55) Hoellwarth, A.; Boehme, M.; Dapprich, S.; Ehlers, A. W.; Gobbi, A.; Jonas, V.; Koehler, K. F.; Stegmann, R.; Veldkamp, A.; Frenking, G. *Chemical Physics Letters* **1993**, ***208***, 237-40.

(56) Hoellwarth, A.; Boehme, M.; Dapprich, S.; Ehlers, A. W.; Gobbi, A.; Jonas, V.; Koehler, K. F.; Stegmann, R.; Veldkamp, A.; Frenking, G. *Chemical Physics Letters* **1994**, ***224***, 603.

(57) Alcami, M.; Mo, O.; Yanez, M.; Cooper, I. L. *Journal of Chemical Physics* **2000**, ***112***, 6131-40.

(58) Lee, T. J.; Dateo, C. E.; Rice, J. E. *Molecular Physics* **1999**, ***96***, 633-43.

(59) Brownsword, R. A.; Hillenkamp, M.; Schmiechen, P.; Volpp, H.-R.; Upadhyaya, H. P. *Journal of Physical Chemistry A* **1998**, ***102***, 4438-43.

(60) Gorbacheva, M. V.; Maiorova, A. F.; Mudretsova, S. N.; Rudnyi, E. B.; Rusin, A. D. *Russian Journal of Physical Chemistry* **1998**, *72*, 340-4.

(61) White, D., "Hg and Zn".

(62) Grade, M.; Hirschwald, W. *Zeitschrift fuer Anorganische und Allgemeine Chemie* **1980**, ***460***, 106-14.

(63) Gleichmann, M. M.; Hess, B. A. *Chemical Physics Letters* **1994**, *227*, 229-34.

(64) Ariya, P. A.; Niki, H.; Harris, G. W.; Anlauf, K. G.; Worthy, D. E. J. *Atmospheric Environment* **1999**, ***33***, 931-8.

(65) Hopper, J. F.; Barrie, L. A.; Silis, A.; Hart, W.; Gallant, A. J.; Dryfhout, H. *Journal of Geophysical Research* **1998**, ***103***, 1481-92.

(66) Leaitch, W. R.; Barrie, L. A.; Bottenheim, J. W.; Li, S. M.; Shepson, P. B.; Muthuramu, K.; Yokouchi, Y. *Journal of Geophysical Research* **1994**, ***99***, 25,499-517.

(67) Rastogi, R. P.; Dubey, B. L.; Agrawal, N. D. *Journal of Inorganic and Nuclear Chemistry* **1975**, ***37***, 1167-72.

(68) Van Loon, L. L.; Mader, E. A.; Scott, S. L. *Journal of Physical Chemistry A* **2001**, ***105***, 3190-5.

(69) Liu, J.; Wang, W.; Peng, A. *Journal of Environmental Science and Health* **2000**, ***A35***, 1859-67.

(70) Horvath, O.; Miko, I. *Journal of Photochemistry and Photobiology, A* **1999**, ***128***, 33-8.